

Old Dominion University

ODU Digital Commons

Mechanical & Aerospace Engineering Theses & Dissertations

Mechanical & Aerospace Engineering

Summer 2012

The Influence of Non-Equilibrium Pressure on Rotating Flows

Irfan Rashid Zardadkhan
Old Dominion University

Follow this and additional works at: https://digitalcommons.odu.edu/mae_etds



Part of the [Aerospace Engineering Commons](#), [Geophysics and Seismology Commons](#), and the [Mechanical Engineering Commons](#)

Recommended Citation

Zardadkhan, Irfan R.. "The Influence of Non-Equilibrium Pressure on Rotating Flows" (2012). Doctor of Philosophy (PhD), Dissertation, Mechanical & Aerospace Engineering, Old Dominion University, DOI: 10.25777/vkqv-br23
https://digitalcommons.odu.edu/mae_etds/166

This Dissertation is brought to you for free and open access by the Mechanical & Aerospace Engineering at ODU Digital Commons. It has been accepted for inclusion in Mechanical & Aerospace Engineering Theses & Dissertations by an authorized administrator of ODU Digital Commons. For more information, please contact digitalcommons@odu.edu.

**THE INFLUENCE OF NON-EQUILIBRIUM PRESSURE
ON ROTATING FLOWS**

by

Irfan Rashid Zardadkhan
B.Sc. January 2001, University of Bahrain, Bahrain
M.Sc. June 2005, University of Bahrain, Bahrain


A Dissertation Submitted to the Faculty of
Old Dominion University in Partial Fulfillment of the
Requirements for the Degree of

DOCTOR OF PHILOSOPHY

AEROSPACE ENGINEERING

OLD DOMINION UNIVERSITY

August 2012

Approved by: 

Robert L. Ash (Director)

Ali Beskok (Member)

Ayodeji Demuren (Member)

Duc Nguyen (Member)

ABSTRACT

THE INFLUENCE OF NON-EQUILIBRIUM PRESSURE ON ROTATING FLOWS

Irfan Rashid Zardadkhan
Old Dominion University, 2012
Director: Robert L. Ash

This study was undertaken to investigate the influence of pressure relaxation on steady, incompressible flows with strong streamline curvature. In the early part of this dissertation research, the significance of non-equilibrium pressure forces in controlling the structure of a steady, two dimensional axial vortex was demonstrated. In order to extend the study of pressure relaxation influences on more complex rotating flows, this dissertation has examined other rotating flow features that can be associated with hurricanes, tornadoes and dust devils. To model these flows, modified boundary layer equations were developed for a fluid column rotating near a solid plane including the influence of non-equilibrium pressure forces. The far-field boundary conditions were inferred using the asymptotic behavior of the governing equations, and the boundary conditions for the axial and radial components of velocity were shown to be dependent on the pressure relaxation coefficient, η_p and the characteristic angular velocity of the rotating fluid column, ω . This research has shown for the first time that the inclusion of non-equilibrium pressure results in a free-standing stagnation plane at the top of a funnel shaped rotating fluid column, which is consistent with observational data for hurricanes, tornadoes and dust devils. It has also been shown that in the absence of non-equilibrium pressure, the stagnation plane for rotating flows cannot be observed. The velocity and pressure distributions resulting from incorporating non-equilibrium pressure effects were

then compared with available observational data for tornadoes and dust devils. The general profiles of the velocity and pressure distributions were found to be in good agreement with physical measurements, which was not possible without introducing empirical turbulence effects, in the absence of non-equilibrium pressure effects.

This work is dedicated to all my family:
my wife for her continuous support and my parents for their endless prayers.

ACKNOWLEDGMENTS

My primary debt of gratitude, of course, goes to my advisor, Prof. Robert L. Ash, who has taken great time out of his hectic schedule on multiple occasions to provide his guidance and share his knowledge with me. It was his encouragement that has rendered this work possible. I would not be able to find words enough to thank him for all what he has done for me over the past few years. I would also like to express my appreciation to Drs. Ali Beskok, Ayodeji Demuren and Duc Nguyen for being on my guidance committee and for their helpful suggestions and support in preparing this dissertation. I would also like to take this opportunity to thank Prof. Taj Mohieldin, whose friendship, guidance and support has been invaluable for me during the past decade. My special thanks go to Dr. Colin Britcher, who has provided his support on various administrative issues. I am also very thankful to all the students of the Aerospace Engineering program, who have helped me on many occasions with very fruitful discussions over the course of my time here.

NOMENCLATURE

English Symbols

a_o	speed of sound
A	Affinity
B	wingspan of an aircraft
e	internal energy
F	non-dimensional radial velocity function
G	non-dimensional swirl velocity function
H	non-dimensional axial velocity function
H_{\max}	non-dimensional stagnation plane height
L	Lagrangian
P	pressure
r, θ, z	cylindrical coordinates
r_{core}	vortex core radius
r_i	inner core radius for multiscale vortex model
r_o	outer core radius for multiscale vortex model
R_o	Rossby number
R_{Γ}	circulation based Reynolds number
s, S	entropy
t	time
T	temperature

u	non-dimensional swirl velocity
\mathbf{v}	velocity vector
ν	specific volume
v_r	radial component of velocity
v_θ	azimuthal component of velocity
v_z	axial component of velocity

Greek Symbols

α, β, φ	Lagrange multipliers
β_i, β_o	constants for the smooth blending vortex model
Γ	circulation
η	non-dimensional height
η_p	pressure relaxation coefficient
η_v	volume viscosity
κ_s^∞	high-frequency adiabatic compressibility
μ	dynamic viscosity
ν	kinematic viscosity
ξ	non-equilibrium progress variable
ρ	density
τ_v, τ_p	volumetric and pressure relaxation times
ω	angular velocity
Ω	potential energy

TABLE OF CONTENTS

	Page
LIST OF TABLES.....	x
LIST OF FIGURES.....	xi
 Chapter	
1. INTRODUCTION.....	1
1.1 Aeronautical and Geophysical Vortices	4
1.1.1 Aircraft Wake Vortices	5
1.1.2 Dust Devils.....	5
1.1.3 Tornadoes.....	7
1.2 Mathematical models for aircraft wake vortices.....	8
1.3 Mathematical Models for Geophysical Vortices.....	13
1.4 The Boedewadt Similarity Velocity Distribution.....	16
 2. GOVERNING EQUATIONS.....	 19
2.1 Derivation of the Governing Equations.....	19
2.1.1 The Lagrangian	20
2.1.2 The Variational Formulation.....	22
2.1.3 Equations of Motion.....	29
2.2 Summary.....	37
 3. THE STRUCTURE OF AN AXIAL VORTEX.....	 38
3.1 Introduction	38
3.2 The Governing Equations.....	39
3.3 Steady-State Solution	42
3.3.1 Properties of the Steady-State Axial Vortex Solution.....	44
3.3.2 The Pressure Distribution.....	45
3.3.3 The Circulation.....	45
3.4 Validation of the Predicted Profiles.....	46
3.4.1 Velocity Profile	46
3.4.2 Pressure Profiles	48
3.4.3 Prediction of the Pressure Relaxation Coefficient using Pressure Deficit.....	50
3.5 Summary.....	52
 4. RIGIDLY ROTATING FLUID COLUMN NEAR THE GROUND	 54
4.1 Introduction	54
4.2 Mathematical Model.....	54
4.2.1 Boundary Conditions.....	57
4.3 Numerical Procedure	60

4.4 The pressure distribution	64
5. ROTATING FLUID COLUMN – RESULTS AND DISCUSSION	66
5.1 The Velocity Distribution.....	66
5.2 The Pressure Distribution	72
5.3 Determination of the Stagnation Plane Elevation.....	72
5.4 Limitations of the Solution.....	76
5.5 Summary.....	77
6. CONCLUSIONS	79
6.1 Summary.....	79
6.2 Future Work.....	81
REFERENCES	82
APPENDICES	86
A. Pressure relaxation coefficient of air	86
B. The MATLAB Code	91
VITA.....	92

LIST OF TABLES

Table	Page
3.1 Estimation of Pressure Relaxation Coefficient using Aircraft Experiments	52
4.1 Stagnation heights for Sinclair (1969) Dust Devils.....	76
A.1 Pressure relaxation coefficient (in μs) for air at selected temperatures and relative humidities.....	90

LIST OF FIGURES

Figure	Page
1.1 Normalized tangential velocity profiles for various vortex models	13
1.2 Flow field showing (A) the viscous core, (B) the outer potential flow (C) the boundary layer away from the core (D) the interaction region (E) stagnation point	15
3.1 Velocity distribution for a vortex filament	47
3.2 Comparison of theoretical velocity profile with Sinclair Dust Devil # 2	48
3.3 Comparison of the normalized tornado pressure profile with the theoretical pressure profile.....	49
3.4 Comparison of dust devil profile with the theoretical pressure profile.	50
4.1 A physical representation of flow rotating near the ground	55
4.2 Comparison of the similarity solutions with (bolder lines) and without (finer lines) pressure relaxation	62
5.1 Streamlines through a vertical slice comparing Boedewadt solution (dashed line) and pressure relaxation solution with $\eta_p\omega=0.1$ (solid line)	68
5.2 Streamlines patterns: (a) for Boedewadt Solution ($\eta_p\omega=0$), and (b) $\eta_p\omega=0.1$	68
5.3 Streamlines through a vertical slice when $\eta_p\omega=0.001$ (a) near the ground (b) near the stagnation plane	69
5.4 Streamlines with $\eta_p\omega=0.001$ (a) near the ground (b) near the stagnation plane	69
5.5 Streamlines through a vertical slice with $\eta_p\omega=0.01$ (a) near the ground (b) near the stagnation plane.....	70
5.6 Streamlines with $\eta_p\omega=0.01$ (a) near the ground (b) near the stagnation plane	70
5.7 Streamlines with $\eta_p\omega=0.01$ showing the rigid column below the stagnation plane.....	71
5.8 Pressure contours within the core	72

5.9 The location of the stagnation point vs. the parameter $\eta_p\omega$	74
---	----

CHAPTER 1

INTRODUCTION

The focus of this research is to further explore the role of non-equilibrium pressure in steady, incompressible flows. Recently, it has been shown that a mechanism for balancing the centrifugal forces that are produced near the centerline of a potential axial vortex with a viscously-coupled rigid-body central core is non-equilibrium pressure (Ash, Zardadkhan & Zuckerwar, 2011); the current work will examine more complex, multi-dimensional flows.

Zuckerwar and Ash (2006, 2009) showed how it was possible to utilize Hamilton's Principal of Least Action, along with appropriate Lagrangian constraints, to introduce non-equilibrium pressure forces in the Navier-Stokes equations. The earlier work was concerned with the development of a more rigorous framework for the determination and use of bulk viscosity in fluids. However, a result of that analysis was the demonstration that there can be two types of bulk viscous effects—the classical dissipative bulk viscosity effect and a second, quasi-reversible, constant-pressure non-equilibrium effect. The two effects cannot be partitioned. Additionally, their derivations showed that there was a constant-volume, quasi-reversible, non-equilibrium pressure effect that could be related linearly to the gradient of the material rate of change of pressure. Detailed derivations of these equations will be presented in Chapter 2.

A non-equilibrium pressure contribution to a steady-state, incompressible fluid flow was considered originally to be nothing more than a curiosity. However, in

Zuckerwar and Ash (2009), it had been shown that a slow-viscous, Stokes flow past a sphere could exhibit non-equilibrium pressure behavior. Consequently, the author of this dissertation was asked to examine the possible non-equilibrium pressure implications on steady, incompressible flows with strong streamline curvature.

The original focus was on axial vortices because of their simplicity and their relevance to a variety of aeronautical and geophysical flows. Those flows are modeled most effectively using cylindrical coordinates. In the process of setting up the axial vortex model, the pressure relaxation contribution was inadvertently switched from the gradient of the material rate of change of pressure to the material rate of change of the pressure gradient. That switch was not consistent with the earlier theoretical derivation but the exclusion of the extra terms associated with the gradient of the material rate of change of pressure can be justified on the basis of acoustic processes as will be shown in Chapter 3. When the material rate of change of the pressure gradient is considered, it will be shown that conservation of the azimuthal component of the momentum equation will result in a balancing term dependent on the pressure relaxation coefficient.

For the case of an axial vortex filament, the governing conservation of momentum equations, including pressure relaxation, simplify to a second order non-linear ordinary differential equation. A logical approach was to solve these equations numerically. Initial numerical experiments were performed by considering a finite flow domain, which is classically known as a Taylor-Couette flow.

The numerical experiments showed that when pressure relaxation was included in the conservation equations, there were slight deviations of the computed swirl velocity

from the theoretical Taylor-Couette velocity distribution. As the inner cylinder radius was decreased significantly and its angular velocity was increased, the numerical solutions showed that unlike the classical solution of the Taylor-Couette vortex, the swirl velocity increased initially from the prescribed inner swirl velocity before decreasing and reaching the swirl velocity of the outer cylinder. Although this type of behavior is not common for Taylor-Couette flows, it is commonly observed in vortex filaments. Once the inner and outer cylinder radii were set to zero and infinity (a very large value for numerical calculations), it was observed that the numerical solution had the characteristics of a typical vortex filament.

For a vortex filament, the swirl velocity goes to zero both at the centerline and at infinity (far-field). Using this information, an analytical solution to the modified equations of motion with pressure relaxation was obtained (Ash, Zardadkhan & Zuckerwar, 2011). Details related to the development of this solution will be presented in Chapter 3. These results motivated the author to study the effects of pressure relaxation on more complex rotating flows.

The axial vortex is an idealized one-dimensional flow. For further exploration of the impacts of pressure relaxation on rotating flows, the backward facing step and the lid driven cavity flow were selected for numerical computations. For steady-state flow simulations, only small deviations were observed in the flow structures when comparing flows with and without non-equilibrium effects. A subtle change in the numerical simulations of flows with non-equilibrium pressure effects was the demonstration that the vortices tended to be more coherent when vortices were stretched in the flow-direction, by increasing the stream-wise component of the flow; rather than forming an elongated

structure, the vortices split forming smaller circular vortices. When unsteady simulations of these flows were attempted, the author was unsuccessful in producing any useful results due to the instability of the numerical methods and further studies of these types of flows were abandoned due to resource constraints.

Since the study of an axial vortex filament had produced useful and interesting results, it was decided to study similar flows, but incorporating axial and radial velocity components. The reason behind selecting these flows was the fact that a number of theoretical and analytical models for these flows were available in the literature. Although axial vortex filaments have been used extensively in the literature to model aerodynamic and geophysical flows, more realistic models are needed that incorporate all three velocity components. The earlier models will be discussed in detail in the following sections.

The turbulent trailing-line vortices created by heavy aircraft are a primary factor controlling the capacity of the busiest international airports. These types of vortices can have long life-times and can pose severe hazards to following aircraft (Gerz, Holzappel, & Darracq, 2002). Although aircraft separation standards are imposed, increases in air traffic require a careful re-examination of the basis for forecasting the potential hazard. Improvements in modeling these vortices can have a direct impact on aviation-related economic growth (Urbarzka & Wilken, 1997).

1.1 Aeronautical and Geophysical Vortices

The study of vortical flows like aircraft wake vortices, tornadoes, hurricanes, dust devils and waterspouts is of major interest in aeronautics, geophysics, meteorology and

fluid mechanics. The ability to model such vortices is important for a variety of applications, including aircraft wake hazard assessment, prediction of tornado and hurricane formation and subsequent trajectories, and assessment of their disaster-causing potential. The importance of non-equilibrium pressure in modeling these types of vortex flows has been discovered only recently and will be the focus of this dissertation. To date, the only axial vortex model that has incorporated non-equilibrium pressure in predicting its structure is the steady, incompressible axial vortex (Ash, Zardadkhan & Zuckerwar, 2011). The research described herein has been concerned with more complex non-equilibrium pressure effects. In order to develop this topic, it has been necessary to examine a wide spectrum of earlier theoretical and empirical vortex research.

1.1.1 Aircraft Wake Vortices

Wake vortices are shed by an aircraft as a consequence of lift generation. Just behind the trailing edge of an aircraft, a strong downward motion exists, whereas in the following region, there is a weak upwards motion. This creates a boundary layer separation and a roll-up of the vortex sheet and all the associated instabilities merge to create the wake vortices. The wake consists of two coherent, counter-rotating vortices of equal strength. The circulation of each axial vortex is proportional to the weight of the aircraft and its wing span (Devenport, Rife, Liapis, & Follin, 1996). The resulting axial vortices are the primary structures responsible for hazardous flight conditions.

1.1.2 Dust Devils

Dust devils are vortices that are generated on hot days over very dry terrain. The dust devil vortex cores can range from 1 meter in diameter to around 10 meters and can

be over 1000 meters tall. They are usually short lived and are rarely a threat to people (Morton, 1966).

A number of dust devil observations were made by Sinclair (1964) in Arizona. He reported that he observed dust devil diameters between 1 meter and 45 meters and heights ranging from 1.5 meters to 1250 meters. The estimated maximum azimuthal velocity within the rigidly-rotating core of these dust devils can be estimated to be in the range of 5 m/s to 10 m/s.

Dust devils are formed when hot air near the surface rises quickly through cooler and lower pressure air. Under the right conditions, the air begins to rotate and as the air rises quickly, the column of hot air is stretched vertically. The rising air causes the air near the ground to be pulled inwards near the base of the vortex. As the air rises in the vortex, it cools, loses buoyancy and stops rising. As the air is sucked into the vortex, it also pulls along dust and debris which make the dust devil visible and also accounts for its name. Dust devils usually last for a few seconds before they are dissipated. Sinclair noted that there has to be an upward axial flow in some sections of the flow but there can also be downward axial flow in the dust devil as well. Dust devils have been observed to rotate both in the clockwise and anticlockwise directions (Brooks, 1959).

Dust devils have also been observed on the surface of Mars (Metzger et al., 1999; Balme & Greely, 2006). Martian dust devils are more intense than terrestrial dust devils, and can be a hundred times larger (Metzger, Carr, Johnson, Parker, & Lemmon, 1999). Martian dust devils have been of interest to scientists because of the threat that they pose to exploration equipment sent to Mars (Balme & Greely, 2006).

1.1.3 Tornadoes

Tornadoes are far more violent than dust devils and far more destructive. Due to the destructive nature of the strong winds in tornadoes, there is virtually no data related to direct measurements within the tornado vortex. Most of the information regarding the structure of tornadoes comes in the form of visual and photographic records. Some measurements of tornadoes have also been made recently using radar systems (Nolan & Farrell, 1999).

Tornadoes are always associated with clouds and storm fronts. Some portion of the vortex below the cloud base is visible as a funnel cloud. These funnels may extend to the ground. The lower part of the vortex is usually seen as a swirling vortex carrying dust, large debris and vegetation. The vortex is relatively narrow near the ground but it spreads out with increasing height, forming a funnel like shape (Morton, 1966).

The most thorough early study of the structure of a tornado was by Hoecker (1960). He studied the Dallas tornado of April 2, 1957 using the imagery captured on film. Using the time rate of advancement of the film and the relative position of the debris suspended in the tornado, he was able to determine the three-dimensional distribution of the velocities in the tornado. The distributions of the tangential velocity profiles, 40 meters above the ground, were generally similar to the vortex models described in section 1.2. The maximum observed tangential velocity for that tornado was 75 m/sec. The core diameter of the vortex increased slowly with height. The maximum observed vertical velocity was 70 m/sec, near the vortex centerline. Above a certain height, the vertical velocity decreased slowly but steadily with height until zero vertical

velocity was achieved at the nominal top of the funnel. This behavior indicates that a stagnation point exists in the tornado at the top of the funnel.

The existence of that type of stagnation condition has usually been associated with vortex breakdown (Ward, 1972). The pressure distribution within a tornado is inferred from the velocity profiles and little is known about relevant temperature profiles within tornadoes.

More recently, Kosiba & Wurman (2010) have used a ground-based velocity tracking method, collecting data from a mobile Doppler radar. Using data from the 1998 Spencer, South Dakota tornado, they estimated the maximum inflow to be 23 m/sec near the ground, with an estimated outflow velocity of 10 m/sec at a height of about 40 meters. The maximum recorded tangential wind velocity was 79 m/sec which reduced gradually to 70 m/sec over a period of few minutes. A maximum downdraft of 60 m/sec was also reported at an altitude of 800 m.

Ward (1972) was able to simulate the dynamic features of a tornado using a laboratory vortex chamber. He was able to simulate the tangential velocity profiles observed in actual tornadoes. He was also able to replicate the downdraft in the vortex core, which he associated with vortex breakdown and the onset of core turbulence.

1.2 Mathematical models for aircraft wake vortices

A number of mathematical models have been developed to describe the radial profiles of the swirl velocity in a rolled-up wake vortex. The most important models will be summarized.

1.2.1 The Rankine vortex

The Rankine vortex (Rankine, 1869) is the simplest axial vortex model. A Rankine vortex incorporates a rigidly-rotating fluid column in the core region, surrounded by a potential vortex. The swirl velocity in the Rankine vortex is given by

$$\begin{aligned} v_{\theta}(r) &= \frac{\Gamma_0}{2\pi r_{core}} \frac{r}{r_{core}} \quad \text{for } r \leq r_{core} \\ v_{\theta}(r) &= \frac{\Gamma_0}{2\pi r} \quad \text{for } r > r_{core} \end{aligned} \quad (1.1)$$

The Rankine vortex can be used effectively to model typical atmospheric phenomena both in the core and in the potential flow regimes, but it cannot predict the transition between the two zones and produces a non-continuous shear stress.

1.2.2 The Lamb-Oseen vortex

The Lamb-Oseen vortex model was developed assuming that the swirl velocity distribution was produced by a potential line vortex that was decaying with time due to viscosity (Lamb, 1932). The potential vortex was used as the initial condition where the centerline velocity was impulsively set to zero. The transient velocity model is given by

$$v_{\theta}(r,t) = \frac{\Gamma_0}{2\pi r} \left[1 - \exp\left(\frac{-r^2}{r_{core}^2(t)}\right) \right], \quad (1.2)$$

where,

$$r_{core}(t) = \sqrt{4\nu t} \quad (1.3)$$

The Lamb-Oseen model is continuous over the entire flow regime, but it is a time-dependent model and is singular along the centerline at zero time.

1.2.3 Hallock-Burnham vortex

An empirical model to define the swirl velocity in a line vortex was developed by Burnham and Hallock (1982) and is given by

$$v_{\theta}(r) = \frac{\Gamma_0}{2\pi r} \frac{r^2}{r^2 + r_{core}^2}. \quad (1.4)$$

That formula represented the best curve fit for aircraft wake vortex velocity profiles compiled over several decades of flight operations.

1.2.4 Adapted Lamb-Oseen vortex

A model was developed by Proctor (1998) for wake vortices which employed the basic Lamb-Oseen vortex model but utilized a correction using Lidar velocity measurements of actual aircraft wake vortices. The swirl velocity for this model is given by

$$v_{\theta}(r) = \frac{\Gamma_0}{2\pi r} \left\{ 1 - \exp \left[-11.8826 \left(\frac{r}{B} \right)^{0.75} \right] \right\} \quad (1.5)$$

where B is the wingspan of the generating aircraft. This model is valid only for $r > r_{core}$.

For smaller radial distances, the Lamb-Oseen model was used.

1.2.5 Smooth blending vortex

The Proctor (1998) adapted model was further improved by Winckelmans, Thirifay & Ploumhans (2000) to produce a continuous, smooth velocity profile given by

$$v_{\theta}(r) = \frac{\Gamma_0}{2\pi r} \left\{ 1 - \exp \left[- \frac{\beta_i \left(\frac{r}{B} \right)^2}{\left\{ 1 + \left[\left(\frac{\beta_i}{\beta_o} \right) \left(\frac{r}{B} \right)^{5/4} \right]^p \right\}^{1/p}} \right] \right\}, \quad (1.6)$$

where β_0 , β_i and p are 10, 500 and 3 respectively. The purpose of this model was to blend the inner viscous and outer potential flow regions and produce a smooth profile with continuous shear stress.

1.2.6 Multiscale vortex model

A model developed by Jacquin et al. (2001), made use of multiple scales. It defined inner and outer core radii and used data from wind tunnel tests to model the tangential velocity distribution for a vortical flow. The model is given by

$$\begin{aligned} v_{\theta}(r) &= \frac{\Gamma_o}{2\pi r_i} \frac{r}{\sqrt{r_i r_o}} \quad \text{for } r \leq r_i \\ v_{\theta}(r) &= \frac{\Gamma_o}{2\pi \sqrt{r_o r}} \quad \text{for } r_i \leq r \leq r_o \\ v_{\theta}(r) &= \frac{\Gamma_o}{2\pi r} \quad \text{for } r > r_o \end{aligned} \quad (1.7)$$

with $r_i \leq 0.01B$ and $r_o \approx 0.1B$. The inner core was defined as the location of the maximum tangential velocity, whereas the outer core was the location where the

maximum circulation was first-approximated. The exact definition of the outer core radius was somewhat arbitrary (Jacquin, Fabre, Geffroy, & Coustols, 2001).

1.2.7 Wood-White Parametric Model

A model based on five parameters: (1) maximum tangential wind speed, (2) radius of maximum tangential wind, and (3-5) three power-law exponents that controlled the shape of the profile peak was developed by Wood & White (2011). The model is an empirical fit and uses root mean square errors to fit the model to the experimental data by adjusting the three power-law exponents in the model.

1.2.8 Comparison of Vortex Filament Models

Some common features of all these models are that the flow in the inner core is dominated by viscosity. The flow in the outer region is free from vorticity and behaves like inviscid or potential flow. The maximum magnitude of the swirl velocity occurs at the core radius.

Although both the Rankine vortex and the Lamb-Oseen vortex are types of exact solutions to the Navier-Stokes equations, they do not adequately model physical vortices (Jacquin, Fabre, Geffroy, & Coustols, 2001). The Rankine vortex is not a continuous function over the entire flow regime and requires different functions for the core region and the potential flow region. The Lamb-Oseen model is continuous, but it cannot be used to model steady-state flows and it decays very rapidly. The vortices represented by the Lamb-Oseen vortex are weak vortices (Morton, 1966). The Hallock-Burnham vortex is an empirical model and is continuous over the full flow regime. The modified Lamb-Oseen model is an empirical fit to the data in the potential flow regime, and is therefore,

more representative of physical flows (Proctor, 1998). The multiscale vortex allows for different core structures with different length scales. The smooth-blending vortex and the Hallock-Burnham model produce results which are very similar (Gerz, Holzapfel, & Darracq, 2002). Figure 1.1 shows a comparison of these different models.

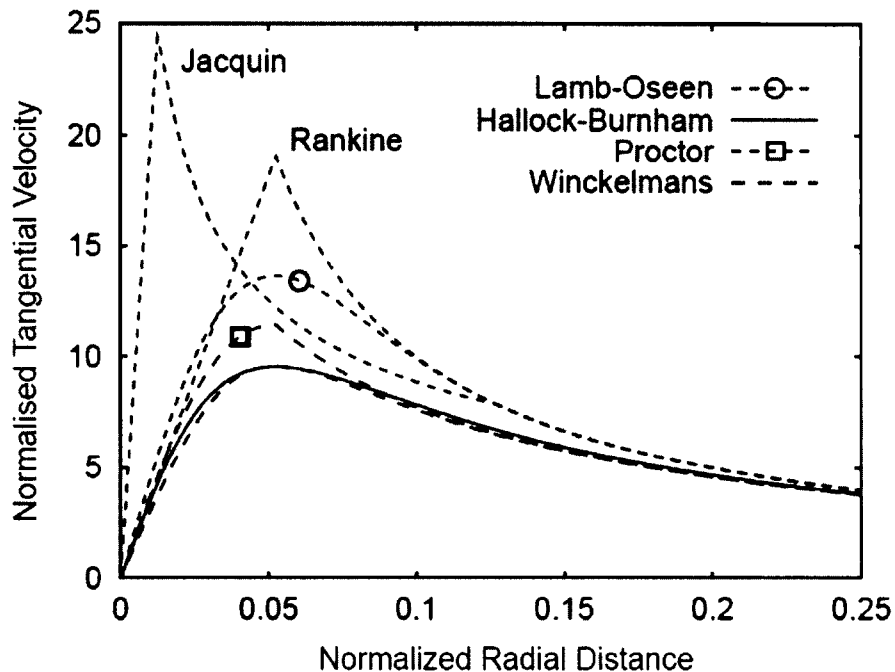


Figure 1.1 Normalized tangential velocity profiles for various vortex models (Gerz, Holzapfel, & Darracq, 2002).

1.3 Mathematical Models for Geophysical Vortices

A considerable amount of work has been carried out attempting to model the flow patterns associated with the formation of various geophysical vortices. A lack of detailed flow measurements has led to debates over the actual structural features of these vortex phenomena. Several numerical models have been proposed to simulate dust devils, waterspouts and tornadoes. These studies have led to the division of the flow regime into

five distinct flow regimes (Hatton, 1975). Figure 1.2 is a crude representation of those five distinct vortical flow regions. Region A is the viscous core and various models exist in the literature to describe this region. The Rankine vortex and Lamb-Oseen models, discussed earlier in Section 1.2, have been used in the literature to describe this region. The Burgers-vortex model assumes the radial velocity varies linearly with radius while the axial velocity varied with the altitude. This work has been replicated by Bellamy-Knights (1974). Sullivan (1959) used a two-cell vortex model to describe the flow in this regime.

Region B is the potential flow region which is sufficiently distant from the viscous core and the ground-coupled regions. The tangential velocity in this region obeys the well-known potential vortex solution, with velocity proportional to $1/r$.

The third region, C, is the boundary layer region away from the viscous core. This region was also studied by Bellamy-Knights (1974) using similarity transformations.

Region D describes the interaction between the rotating viscous fluid core and the stationary ground plane beneath it. Most of the models used to describe viscous core region A fail to implement a no-slip boundary condition at the ground plane and therefore are not able to model this flow region. The similarity solution proposed by Boedewadt (1940) can be used to describe this flow. This model will be discussed in more detail in the next section.

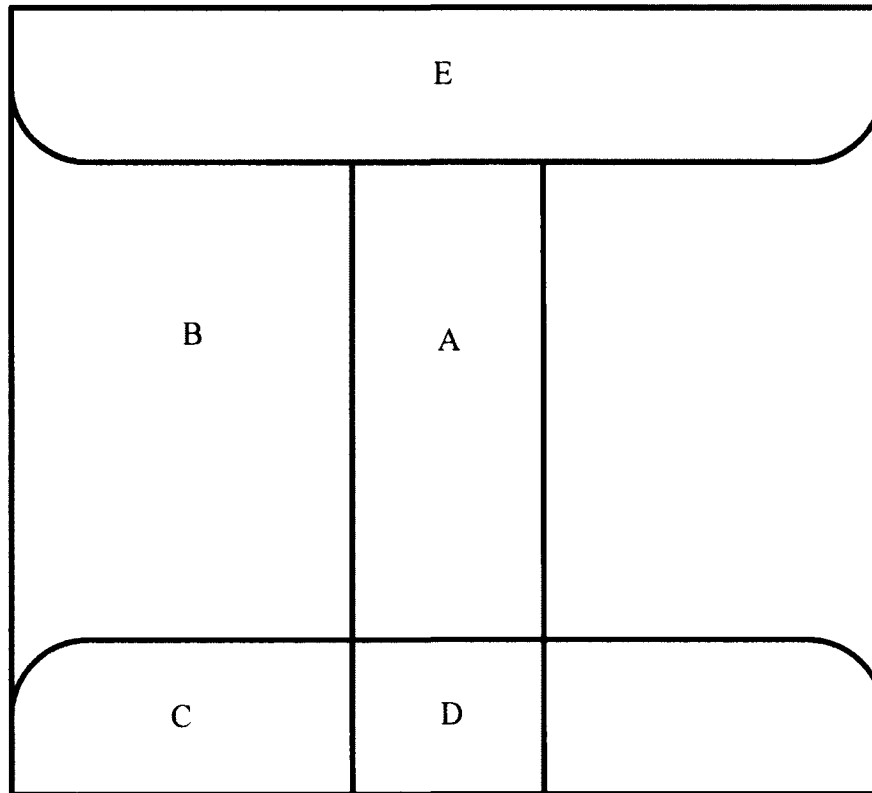


Figure 1.2 Flow field showing (A) the viscous core, (B) the outer potential flow (C) the boundary layer away from the core (D) the interaction region (E) stagnation point.

Region E, is the stagnation region which has been observed in many of these geophysical flow types (Hoecker, 1960; Sinclair 1963; Ward, 1972). This region has not received significant attention. Hatton (1975) modified the boundary conditions on the ground and the stagnation point away from the ground to obtain a solution that demonstrated the existence of a stagnation point. He concluded that the location of the stagnation point depended on a parameter that was proportional to the angular velocity of the viscous core above the interaction region. Similar studies by Raymond & Rao (1978) also showed that if the flow was assumed to be turbulent, then with specific combinations of Reynolds numbers and Rossby numbers, a stagnation point could be observed. Both

these models relied on the assumption that the flow was turbulent and the use of slip boundary conditions on the ground were required to achieve the stagnation point. Since both these models were based on the Bellamy-Knight model, they are transient and cannot be used to describe steady-state vortices.

1.4 The Boedewadt Similarity Velocity Distribution

Regions A and D in Figure 1.2, can be best described as a near-rigid column of fluid, rotating above a solid boundary. This type of hypothetical flow was first analyzed by Boedewadt using similarity transformations (Boedewadt, 1940). A common feature of this modeling approach is that the velocity components are represented in cylindrical coordinates. The steady-state, axisymmetric governing equations in cylindrical coordinates are given by

$$v_r \frac{\partial v_r}{\partial r} - \frac{v_\theta^2}{r} + v_z \frac{\partial v_r}{\partial z} = -\frac{1}{\rho} \frac{\partial P}{\partial r} + \nu \left(\frac{\partial^2 v_r}{\partial r^2} + \frac{1}{r} \frac{\partial v_r}{\partial r} - \frac{v_r}{r^2} + \frac{\partial^2 v_r}{\partial z^2} \right) \quad (1.8)$$

$$v_r \frac{\partial v_\theta}{\partial r} + \frac{v_r v_\theta}{r} + v_z \frac{\partial v_\theta}{\partial z} = \nu \left(\frac{\partial^2 v_\theta}{\partial r^2} + \frac{1}{r} \frac{\partial v_\theta}{\partial r} - \frac{v_\theta}{r^2} + \frac{\partial^2 v_\theta}{\partial z^2} \right) \quad (1.9)$$

$$v_r \frac{\partial v_z}{\partial r} + v_z \frac{\partial v_z}{\partial z} = -\frac{1}{\rho} \frac{\partial P}{\partial z} + \nu \left\{ \frac{\partial^2 v_z}{\partial r^2} + \frac{1}{r} \frac{\partial v_z}{\partial r} + \frac{\partial^2 v_z}{\partial z^2} \right\} \quad (1.10)$$

Boedewadt utilized the following similarity variable and non-dimensional velocity functions:

$$\eta = z \sqrt{\frac{\omega}{\nu}}, \quad v_r = r\omega F(\eta), \quad v_\theta = r\omega G(\eta), \quad v_z = \sqrt{\nu\omega} H(\eta). \quad (1.11)$$

For a frictionless flow at a large distance from the wall, the radial pressure gradient can be computed using

$$\frac{1}{\rho} \frac{\partial p}{\partial r} = r\omega^2, \quad (1.12)$$

and using boundary layer theory, it is assumed that the same pressure gradient acts in the viscous layer close to the solid plane. We can rewrite the governing equations as a set of ordinary differential equations given by

$$F^2 - G^2 + HF' - F'' + 1 = 0, \quad (1.13)$$

$$2FG + G'H - G'' = 0, \quad (1.14)$$

$$2F + H' = 0. \quad (1.15)$$

The boundary conditions imposed on the components of flow are no-slip conditions, hence all components of flow are zero. Away from the ground, Boedewadt (1940), suggested that the azimuthal component of flow reaches the constant free stream value, whereas there is no radial inflow and outflow. Since there is no radial component of flow, the continuity suggests that the axial component reaches a constant value. The boundary conditions are then given by:

$$\begin{aligned} F(0) = 0, \quad G(0) = 0, \quad H(0) = 0, \\ F(\infty) = 0, \quad G(\infty) = 1. \end{aligned} \quad (1.16)$$

The non-linear ordinary differential equations (1.13)-(1.15) with the boundary conditions (1.16) were solved numerically by Boedewadt (1940) and an improved numerical

solution was developed by Rogers and Lance (1963)^{*}. These boundary layer equations will be revised to include non-equilibrium pressure forces in Chapter 4.

^{*} Their tabulated solutions for Boedewadt's functions will henceforth be referred to as *Boedewadt's solutions*.

CHAPTER 2

GOVERNING EQUATIONS

In this chapter, the equations governing fluid motion including non-equilibrium pressure contributions will be developed. The procedure for obtaining the governing equations with the non-equilibrium pressure was developed originally by Zuckerwar and Ash (2006).

2.1 Derivation of the Governing Equations

The governing equations of motion can be developed from the thermodynamic relationship between internal energy, entropy and specific volume for a single substance:

$$de = Tds - Pd\mathcal{V} = Tds + \frac{P}{\rho^2} d\rho. \quad (2.1)$$

This relationship defines the variation of the specific internal energy when the variation is along a path that can be described in terms of changes in entropy and specific volume which is based on the irreversible thermodynamic studies carried out by Miexner, (1952) who examined acoustic absorption and sound generation in fluids when irreversible thermodynamic effects were included. Those early studies introduced and defined affinity (A), along with a non-equilibrium progress variable (ξ), in order to represent differential changes in specific internal energy along thermodynamic paths that departed from the conventional quasi-steady equilibrium paths, i.e.

$$de = Tds - Pd\mathcal{V} - Ad\xi. \quad (2.2)$$

Meixner's work showed that since thermodynamic paths involving any pair of independent variables were possible, non-equilibrium paths were also possible; therefore, the following thermodynamic paths could be considered:

$$de = Tds - Ad\xi, \quad (2.3)$$

$$de = -Pdv - Ad\xi = \frac{P}{\rho^2}d\rho - Ad\xi. \quad (2.4)$$

By fixing different pairs of thermodynamic variables as constants, the following exact relationships or identities can be obtained:

$$T = \left(\frac{\partial e}{\partial s} \right)_{\nu, \xi}, \quad (2.5)$$

$$A = - \left(\frac{\partial e}{\partial \xi} \right)_{s, \nu}, \quad (2.6)$$

$$P = - \left(\frac{\partial e}{\partial \nu} \right)_{s, \xi}. \quad (2.7)$$

These relationships suggest that non-equilibrium pressure and temperature can be sustained in a thermodynamic system. These non-equilibrium states have been studied by Casas-Vázquez & Jou, (2003).

2.1.1 The Lagrangian

Non-equilibrium temperature and pressure effects can be incorporated in the equations of motion by invoking Hamilton's Principle of Least Action. The Lagrangian can be represented using fluid mechanical notation while assuming that internal energy,

along with the kinetic and potential energy, can contribute to the optimal least action path. Letting Ω represent the potential energy function, the Lagrangian can be represented as:

$$L = \rho \left[\frac{v_k^2}{2} - \Omega - e(T, P, \xi) \right]. \quad (2.8)$$

This approach was used by Serrin, (1959) to develop the governing equations for inviscid, compressible fluid flow. Serrin used Lagrange multipliers to impose conservation of mass, minimum entropy and particle identity constraints. In order to incorporate non-equilibrium effects, the particle identity constraint has been replaced with a non-equilibrium conservation of reacting species constraint. The conservation of mass constraint is given by:

$$\frac{D\rho}{Dt} + \rho \frac{\partial v_k}{\partial x_k} = 0. \quad (2.9)$$

The minimum entropy of a quasi-reversible non-equilibrium process constraint is given by:

$$\frac{Ds}{Dt} = 0. \quad (2.10)$$

The conservation of reacting species constraint employed to introduce non-equilibrium thermodynamic states is given in terms of the progress variable and its affinity as:

$$\frac{D\xi}{Dt} = LA, \quad (2.11)$$

where L is a constant.

2.1.2 The Variational Formulation

Using Lagrange multipliers φ , α and β in order to impose the desired constraints in the Lagrangian statement for Hamilton's Principle of Least Action, the following variation results:

$$\delta \int_{t_0}^{t_1} \iiint_V \left[\frac{1}{2} \rho v_k v_k - \rho (e + \Omega) - \varphi \left(\frac{D\rho}{Dt} + \rho \frac{\partial v_k}{\partial x_k} \right) - \alpha \rho \left(\frac{D\xi}{Dt} - LA \right) - \beta \rho \frac{Ds}{Dt} \right] dV dt = 0. \quad (2.12)$$

For the sake of convenience, the integral is represented as I and the integrand is called F , and Equation 2.12 can be rewritten:

$$\delta I = \delta \int_{t_0}^{t_1} \iiint_V F(\mathbf{x}, t, \rho, \mathbf{v}, s, \xi) dV dt = 0. \quad (2.13)$$

The Einstein summation convention has been used to write F as:

$$F = \frac{1}{2} \rho v_k v_k - \rho (e + \Omega) - \varphi \left(\frac{D\rho}{Dt} + \rho \frac{\partial v_k}{\partial x_k} \right) - \alpha \rho \left(\frac{D\xi}{Dt} - LA \right) - \beta \rho \frac{Ds}{Dt}. \quad (2.14)$$

Following the developments of Herivel (1959), the variation in F can be written:

$$\begin{aligned} \delta F = & \frac{\partial F}{\partial \rho} \delta \rho + \frac{\partial F}{\partial \left(\frac{\partial \rho}{\partial t} \right)} \delta \left(\frac{\partial \rho}{\partial t} \right) + \frac{\partial F}{\partial \left(\frac{\partial \rho}{\partial x_j} \right)} \delta \left(\frac{\partial \rho}{\partial x_j} \right) + \frac{\partial F}{\partial v_j} \delta v_j + \\ & + \frac{\partial F}{\partial \left(\frac{\partial v_k}{\partial x_k} \right)} \delta \left(\frac{\partial v_k}{\partial x_k} \right) + \frac{\partial F}{\partial s} \delta s + \frac{\partial F}{\partial \left(\frac{\partial s}{\partial t} \right)} \delta \left(\frac{\partial s}{\partial t} \right) + \frac{\partial F}{\partial \left(\frac{\partial s}{\partial x_j} \right)} \delta \left(\frac{\partial s}{\partial x_j} \right) + \\ & + \frac{\partial F}{\partial \xi} \delta \xi + \frac{\partial F}{\partial \left(\frac{\partial \xi}{\partial t} \right)} \delta \left(\frac{\partial \xi}{\partial t} \right) + \frac{\partial F}{\partial \left(\frac{\partial \xi}{\partial x_j} \right)} \delta \left(\frac{\partial \xi}{\partial x_j} \right). \end{aligned} \quad (2.15)$$

It is convenient to examine the independent variations in the velocity components, density, entropy and the progress variable departures separately. The variation with respect to density yields:

$$\frac{\partial F}{\partial \rho} = \frac{v_k v_k}{2} - (e + \Omega) - \rho \left(\frac{\partial u}{\partial \rho} \right)_{s, \xi} - \varphi \frac{\partial v_k}{\partial x_k} - \alpha \left(\frac{D\xi}{Dt} - LA \right) - \beta \frac{Ds}{Dt}. \quad (2.16)$$

Using Eqs. (2.10) and (2.11), this variational relationship can be simplified as:

$$\frac{\partial F}{\partial \rho} = \frac{v_k v_k}{2} - (e + \Omega) - \rho \left(\frac{\partial e}{\partial \rho} \right)_{s, \xi} - \varphi \frac{\partial v_k}{\partial x_k}. \quad (2.17)$$

In addition,
$$\frac{\partial F}{\partial \left(\frac{\partial \rho}{\partial t} \right)} = -\varphi. \quad (2.18)$$

Interchanging the order of the volume and time integrals results in the integral relation:

$$\int_{t_0}^{t_1} \iiint_V \frac{\partial F}{\partial \left(\frac{\partial \rho}{\partial t} \right)} \delta \left(\frac{\partial \rho}{\partial t} \right) dV dt = \iiint_V \int_{t_0}^{t_1} \frac{\partial F}{\partial \left(\frac{\partial \rho}{\partial t} \right)} \delta \left(\frac{\partial \rho}{\partial t} \right) dt dV. \quad (2.19)$$

By interchanging the order of differentiation and variation within the last integral, the following relationship results:

$$\iiint_V \int_{t_0}^{t_1} \frac{\partial F}{\partial \left(\frac{\partial \rho}{\partial t} \right)} \frac{\partial}{\partial t} (\delta \rho) dt dV. \quad (2.20)$$

Then, integrating the inner time integral in (2.19) by parts

$$\frac{\partial F}{\partial \left(\frac{\partial \rho}{\partial t} \right)} \delta \rho \Big|_{t_0}^{t_1} - \int_{t_0}^{t_1} \frac{\partial}{\partial t} \left[\frac{\partial F}{\partial \left(\frac{\partial \rho}{\partial t} \right)} \right] \delta \rho dt = \quad (2.21)$$

$$= \int_{t_0}^{t_1} \frac{\partial \phi}{\partial t} \delta \rho dt. \quad (2.22)$$

By making use of Eq. (2.21), Eq. (2.18) can be rewritten:

$$\int_{t_0}^{t_1} \iiint_V \frac{\partial F}{\partial \left(\frac{\partial \rho}{\partial t} \right)} \delta \left(\frac{\partial \rho}{\partial t} \right) dV dt = \iiint_V \int_{t_0}^{t_1} \frac{\partial \phi}{\partial t} \delta \rho dV dt. \quad (2.23)$$

Next,

$$\frac{\partial F}{\partial \left(\frac{\partial \rho}{\partial x_i} \right)} = -\phi v_i. \quad (2.24)$$

Using similar procedures to the previous integral, the following integral can be evaluated

$$\int_{t_0}^{t_1} \iiint_V \frac{\partial F}{\partial \left(\frac{\partial \rho}{\partial x_j} \right)} \delta \left(\frac{\partial \rho}{\partial x_j} \right) dV dt = \quad (2.25)$$

$$= \int_{t_0}^{t_1} \iiint_V \frac{\partial}{\partial x_i} (\phi v_i) \delta \rho dV dt. \quad (2.26)$$

Now by adding (2.16), (2.22) and (2.25), the variation of density translates to the requirement that

$$\frac{v_k v_k}{2} - (e + \Omega) - \rho \left(\frac{\partial e}{\partial \rho} \right)_{s,\xi} + \varphi \frac{\partial v_k}{\partial x_k} - \frac{\partial \varphi}{\partial t} - \frac{\partial}{\partial x_k} (v_k \phi) = 0, \quad (2.27)$$

or,

$$\frac{D\varphi}{Dt} = \frac{1}{2} v_k v_k - (e + \Omega) - \rho \left(\frac{\partial e}{\partial \rho} \right)_{s,\xi}. \quad (2.28)$$

And since

$$de = Tds + \frac{P}{\rho^2} d\rho \Rightarrow \rho \left(\frac{\partial e}{\partial \rho} \right)_{s,\xi} = \frac{P}{\rho}, \quad (2.29)$$

Eq. (2.28) can be rewritten:

$$\frac{D\varphi}{Dt} = \frac{1}{2} v_k v_k - (e + \Omega) - \frac{P}{\rho}. \quad (2.30)$$

The variations of the individual velocity components were considered next. The derivatives with respect to the k th velocity component can be written:

$$\frac{\partial F}{\partial v_k} = \rho v_k - \rho \alpha \frac{\partial \xi}{\partial x_k} - \rho \beta \frac{\partial s}{\partial x_k} - \varphi \frac{\partial \rho}{\partial x_k}, \quad (2.31)$$

while the derivative with respect to the divergence of the velocity becomes:

$$\frac{\partial F}{\partial \left(\frac{\partial v_k}{\partial x_k} \right)} = -\rho \varphi, \quad (2.32)$$

and
$$\frac{\partial F}{\partial \left(\frac{\partial v_k}{\partial t} \right)} = 0. \quad (2.33)$$

Now,

$$\iiint_{\mathcal{V}} \frac{\partial F}{\partial \left(\frac{\partial v_1}{\partial x_1} \right)} \delta \left(\frac{\partial v_1}{\partial x_1} \right) d\mathcal{V} = - \iiint_{\mathcal{V}} \frac{\partial}{\partial x_1} \left[\frac{\partial F}{\partial \left(\frac{\partial v_1}{\partial x_1} \right)} \right] \delta v_1 d\mathcal{V} = \iiint_{\mathcal{V}} \frac{\partial}{\partial x_1} (\rho \phi) \delta v_1 d\mathcal{V}. \quad (2.34)$$

Hence, the variation of velocity component, v_k , requires that:

$$\rho v_k - \rho \alpha \frac{\partial \xi}{\partial x_k} - \rho \beta \frac{\partial s}{\partial x_k} + \varphi \frac{\partial \rho}{\partial x_k} - \frac{\partial \rho \phi}{\partial x_k} = 0, \quad (2.35)$$

or,

$$v_k = \alpha \frac{\partial \xi}{\partial x_k} + \beta \frac{\partial s}{\partial x_k} + \frac{\partial \phi}{\partial x_k}. \quad (2.36)$$

Next,

$$\frac{\partial F}{\partial s} = -\rho \left(\frac{\partial e}{\partial s} \right)_{\rho, \xi}. \quad (2.37)$$

Using Eq. (2.5),

$$\frac{\partial F}{\partial s} = -\rho T, \quad (2.38)$$

$$\frac{\partial F}{\partial \left(\frac{\partial s}{\partial t} \right)} = -\rho\beta, \quad (2.39)$$

and

$$\frac{\partial F}{\partial \left(\frac{\partial s}{\partial x_k} \right)} = -\rho v_k \beta. \quad (2.40)$$

Employing integration by parts similar to Eq. (2.22) and Eq. (2.24), the variation of entropy requires that

$$\rho T - \frac{\partial}{\partial t}(\rho\beta) - \frac{\partial}{\partial x_k}(\rho v_k \beta) = 0, \quad (2.41)$$

or,

$$\rho T = \frac{\partial}{\partial t}(\rho\beta) + v_k \frac{\partial}{\partial x_k}(\rho\beta) + \rho\beta \frac{\partial v_k}{\partial x_k}, \quad (2.42)$$

$$\Rightarrow \rho T = \frac{D}{Dt}(\rho\beta) + \rho\beta \frac{\partial v_k}{\partial x_k} \Rightarrow \rho T = \rho \frac{D\beta}{Dt} + \beta \frac{D\rho}{Dt} + \rho\beta \frac{\partial v_k}{\partial x_k}, \quad (2.43)$$

$$\Rightarrow \rho T = \rho \frac{D\beta}{Dt} + \beta \left(\frac{D\rho}{Dt} + \rho \frac{\partial v_k}{\partial x_k} \right). \quad (2.44)$$

Using Eq. (2.9),

$$\rho T = \rho \frac{D\beta}{Dt} \Rightarrow T = \frac{D\beta}{Dt}. \quad (2.45)$$

Finally,

$$\frac{\partial F}{\partial \xi} = -\rho \left(\frac{\partial e}{\partial \xi} \right)_{\rho, s}. \quad (2.46)$$

Using Eq. (2.6),

$$\frac{\partial F}{\partial \xi} = -\rho A, \quad (2.47)$$

$$\frac{\partial F}{\partial \left(\frac{\partial \xi}{\partial t} \right)} = -\rho \alpha, \quad (2.48)$$

$$\text{and } \frac{\partial F}{\partial \left(\frac{\partial \xi}{\partial x_k} \right)} = -\rho v_k \alpha. \quad (2.49)$$

Employing integration by parts similar to Eq. (2.22) and Eq. (2.24), the variation of the progress variable requires that

$$\rho A - \frac{\partial}{\partial t}(\rho \alpha) - \frac{\partial}{\partial x_k}(\rho v_k \alpha) = 0. \quad (2.50)$$

Rearranging,

$$\rho A = \frac{\partial}{\partial t}(\rho \alpha) + \rho \alpha \frac{\partial v_k}{\partial x_k} + v_k \frac{\partial}{\partial x_k}(\rho \alpha), \quad (2.51)$$

and using the definition of the material derivative,

$$\rho A = \frac{D}{Dt}(\rho \alpha) + \rho \alpha \frac{\partial v_k}{\partial x_k} \Rightarrow \rho A = \rho \frac{D\alpha}{Dt} + \alpha \frac{D\rho}{Dt} + \rho \alpha \frac{\partial v_k}{\partial x_k}. \quad (2.52)$$

Gathering all the terms and making use of the continuity constraint,

$$\rho A = \rho \frac{D\alpha}{Dt} + \alpha \left(\frac{D\rho}{Dt} + \rho \frac{\partial v_k}{\partial x_k} \right) \Rightarrow A = \frac{D\alpha}{Dt}. \quad (2.53)$$

2.1.3 Equations of Motion

The equations of motion can now be developed incorporating the requirements resulting from the variations of density, velocity components, entropy and the progress variable. From the variation of density Eq. (2.30),

$$\frac{\partial \varphi}{\partial t} + v_k \frac{\partial \varphi}{\partial x_i} = \frac{1}{2} v_k v_k - (e + \Omega) - \frac{P}{\rho}. \quad (2.54)$$

Subtracting $v_k v_k$ from both sides,

$$\frac{\partial \varphi}{\partial t} + v_k \left(\frac{\partial \varphi}{\partial x_i} - v_k \right) = -\frac{1}{2} v_k v_k - (e + \Omega) - \frac{P}{\rho}. \quad (2.55)$$

Substituting from the variation of velocity components Eq. (2.36)

$$\frac{\partial \varphi}{\partial t} - v_k \left(\alpha \frac{\partial \xi}{\partial x_k} + \beta \frac{\partial s}{\partial x_k} \right) = -\frac{1}{2} v_k v_k - (e + \Omega) - \frac{P}{\rho}. \quad (2.56)$$

Now, taking the gradient of this expression with respect to x_i , yields:

$$\frac{\partial}{\partial x_i} \frac{\partial \varphi}{\partial t} - \frac{\partial}{\partial x_i} \left[v_k \left(\alpha \frac{\partial \xi}{\partial x_k} + \beta \frac{\partial s}{\partial x_k} \right) \right] = -\frac{\partial}{\partial x_i} \left(\frac{v_k v_k}{2} \right) - \frac{\partial}{\partial x_i} (e + \Omega) - \frac{\partial}{\partial x_i} \left(\frac{P}{\rho} \right). \quad (2.57)$$

By employing the vector identity:

$$\frac{\partial}{\partial x_i} \left(\frac{v_k v_k}{2} \right) = v_k \frac{\partial v_i}{\partial x_k} + \varepsilon_{ijk} v_j \left(\varepsilon_{kmn} \frac{\partial v_n}{\partial x_m} \right), \quad (2.58)$$

and substituting for $\frac{\partial v_n}{\partial x_m}$ from Eq. (2.36),

$$\frac{\partial v_n}{\partial x_m} = \frac{\partial^2 \varphi}{\partial x_m \partial x_n} + \frac{\partial}{\partial x_m} \left(\alpha \frac{\partial \xi}{\partial x_n} \right) + \frac{\partial}{\partial x_m} \left(\beta \frac{\partial s}{\partial x_n} \right), \quad (2.59)$$

then using the Levi-Civita to Kronecker delta relationship,

$\varepsilon_{ijk} \varepsilon_{kmn} = \varepsilon_{ijk} \varepsilon_{mnk} = \delta_{im} \delta_{jn} - \delta_{in} \delta_{jm}$, Eq (2.58) can be rewritten:

$$\begin{aligned} \frac{\partial}{\partial x_i} \left(\frac{v_k v_k}{2} \right) &= v_k \frac{\partial v_i}{\partial x_k} + \\ &+ \left(\delta_{im} \delta_{jn} - \delta_{in} \delta_{jm} \right) \left[v_j \frac{\partial^2 \varphi}{\partial x_m \partial x_n} + v_j \frac{\partial}{\partial x_m} \left(\alpha \frac{\partial \xi}{\partial x_n} \right) + v_j \frac{\partial}{\partial x_m} \left(\beta \frac{\partial s}{\partial x_n} \right) \right]. \end{aligned} \quad (2.60)$$

Upon applying the properties of the Kronecker delta function,

$$\frac{\partial}{\partial x_i} \left(\frac{v_k v_k}{2} \right) = v_k \frac{\partial v_i}{\partial x_k} + v_j \frac{\partial}{\partial x_i} \left(\alpha \frac{\partial \xi}{\partial x_j} + \beta \frac{\partial s}{\partial x_j} \right) - v_j \frac{\partial}{\partial x_j} \left(\alpha \frac{\partial \xi}{\partial x_i} + \beta \frac{\partial s}{\partial x_i} \right). \quad (2.61)$$

Substituting Eq. (2.61) into Eq. (2.57)

$$\begin{aligned} \frac{\partial}{\partial t} \frac{\partial \varphi}{\partial x_i} - v_k \frac{\partial}{\partial x_i} \left(\alpha \frac{\partial \xi}{\partial x_k} + \beta \frac{\partial s}{\partial x_k} \right) - \frac{\partial v_k}{\partial x_i} \left(\alpha \frac{\partial \xi}{\partial x_k} + \beta \frac{\partial s}{\partial x_k} \right) &= -v_k \frac{\partial v_i}{\partial x_k} + \\ + v_k \frac{\partial}{\partial x_k} \left(\alpha \frac{\partial \xi}{\partial x_i} + \beta \frac{\partial s}{\partial x_i} \right) - v_k \frac{\partial}{\partial x_i} \left(\alpha \frac{\partial \xi}{\partial x_k} + \beta \frac{\partial s}{\partial x_k} \right) &+ \\ - \frac{\partial e}{\partial x_i} - \frac{\partial \Omega}{\partial x_i} + \frac{P}{\rho^2} \frac{\partial \rho}{\partial x_i} - \frac{1}{\rho} \frac{\partial P}{\partial x_i}. \end{aligned} \quad (2.62)$$

Now, differentiating Eq. (2.36) with respect to time yields

$$\frac{\partial}{\partial t} \frac{\partial \varphi}{\partial x_i} = \frac{\partial v_i}{\partial t} - \frac{\partial}{\partial t} \left(\alpha \frac{\partial \xi}{\partial x_i} + \beta \frac{\partial s}{\partial x_i} \right). \quad (2.63)$$

Substituting this relationship into Eq. (2.62)

$$\begin{aligned} & \frac{\partial v_i}{\partial t} - \frac{\partial}{\partial t} \left(\alpha \frac{\partial \xi}{\partial x_i} + \beta \frac{\partial s}{\partial x_i} \right) - v_k \frac{\partial}{\partial x_k} \left(\alpha \frac{\partial \xi}{\partial x_i} + \beta \frac{\partial s}{\partial x_k} \right) + \\ & - \frac{\partial v_k}{\partial x_i} \left(\alpha \frac{\partial \xi}{\partial x_k} + \beta \frac{\partial s}{\partial x_k} \right) = -v_k \frac{\partial v_i}{\partial x_k} + \\ & + v_k \frac{\partial}{\partial x_k} \left(\alpha \frac{\partial \xi}{\partial x_i} + \beta \frac{\partial s}{\partial x_i} \right) - v_k \frac{\partial}{\partial x_i} \left(\alpha \frac{\partial \xi}{\partial x_k} + \beta \frac{\partial s}{\partial x_k} \right) + \\ & - \frac{\partial e}{\partial x_i} - \frac{\partial \Omega}{\partial x_i} + \frac{P}{\rho^2} \frac{\partial \rho}{\partial x_i} - \frac{1}{\rho} \frac{\partial P}{\partial x_i}, \end{aligned} \quad (2.64)$$

$$\begin{aligned} \Rightarrow & \frac{Dv_i}{Dt} - \frac{D}{Dt} \left(\alpha \frac{\partial \xi}{\partial x_i} + \beta \frac{\partial s}{\partial x_i} \right) - \frac{\partial v_k}{\partial x_i} \left(\alpha \frac{\partial \xi}{\partial x_k} + \beta \frac{\partial s}{\partial x_k} \right) = + \\ & - \frac{\partial e}{\partial x_i} - \frac{\partial \Omega}{\partial x_i} + \frac{P}{\rho^2} \frac{\partial \rho}{\partial x_i} - \frac{1}{\rho} \frac{\partial P}{\partial x_i}. \end{aligned} \quad (2.65)$$

Hence,

$$\frac{D}{Dt} \left(\alpha \frac{\partial \xi}{\partial x_i} \right) + \frac{\partial v_k}{\partial x_i} \alpha \frac{\partial \xi}{\partial x_k} = \frac{\partial \xi}{\partial x_i} \frac{D\alpha}{Dt} + \alpha \frac{D}{Dt} \left(\frac{\partial \xi}{\partial x_i} \right) + \frac{\partial v_k}{\partial x_i} \alpha \frac{\partial \xi}{\partial x_k}. \quad (2.65)$$

Using Eq. (2.53),

$$\begin{aligned}
& A \frac{\partial \xi}{\partial x_i} + \alpha \frac{D}{Dt} \left(\frac{\partial \xi}{\partial x_i} \right) + \frac{\partial v_k}{\partial x_i} \alpha \frac{\partial \xi}{\partial x_k}, \\
& = A \frac{\partial \xi}{\partial x_i} + \alpha \left[\frac{\partial}{\partial t} \left(\frac{\partial \xi}{\partial x_i} \right) + v_k \frac{\partial}{\partial x_k} \left(\frac{\partial \xi}{\partial x_i} \right) \right] + \frac{\partial v_k}{\partial x_i} \alpha \frac{\partial \xi}{\partial x_k}, \tag{2.66}
\end{aligned}$$

$$\begin{aligned}
& = A \frac{\partial \xi}{\partial x_i} + \alpha \left[\frac{\partial}{\partial x_i} \left(\frac{\partial \xi}{\partial t} + v_k \frac{\partial \xi}{\partial x_k} \right) \right] - \frac{\partial v_k}{\partial x_i} \frac{\partial \xi}{\partial x_k} + \frac{\partial v_k}{\partial x_i} \alpha \frac{\partial \xi}{\partial x_k}, \\
& = A \frac{\partial \xi}{\partial x_i} + \alpha \frac{\partial}{\partial x_i} \left(\frac{D\xi}{Dt} \right). \tag{2.67}
\end{aligned}$$

Similarly,

$$\frac{D}{Dt} \left(\beta \frac{\partial s}{\partial x_i} \right) + \frac{\partial v_k}{\partial x_i} \beta \frac{\partial s}{\partial x_k} = T \frac{\partial s}{\partial x_i} + \beta \frac{\partial}{\partial x_i} \left(\frac{Ds}{Dt} \right). \tag{2.68}$$

Substituting Eq. (2.67) and (2.68) into Eq. (2.65),

$$\begin{aligned}
& \frac{Dv_i}{Dt} - A \frac{\partial \xi}{\partial x_i} - \alpha \frac{\partial}{\partial x_i} \left(\frac{D\xi}{Dt} \right) - T \frac{\partial s}{\partial x_i} - \beta \frac{\partial}{\partial x_i} \left(\frac{Ds}{Dt} \right) = + \\
& - \frac{\partial e}{\partial x_i} - \frac{\partial \Omega}{\partial x_i} + \frac{P}{\rho^2} \frac{\partial \rho}{\partial x_i} - \frac{1}{\rho} \frac{\partial P}{\partial x_i}. \tag{2.69}
\end{aligned}$$

Using Eq (2.2) and Eq. (2.10) yields the relationship

$$\frac{Dv_i}{Dt} = - \frac{\partial \Omega}{\partial x_i} - \frac{1}{\rho} \frac{\partial P}{\partial x_i} + \alpha \frac{\partial}{\partial x_i} \left(\frac{D\xi}{Dt} \right). \tag{2.70}$$

Then, rewriting Eq. (2.70) in vector form:

$$\rho \frac{D\mathbf{v}}{Dt} = -\rho \nabla \Omega - \nabla P + \rho \alpha \nabla \left(\frac{D\xi}{Dt} \right). \tag{2.71}$$

This equation can be recognized as the inviscid conservation of momentum equation *with an extra non-equilibrium term*. By utilizing Hamilton's Principal of Least Action and the three Lagrange-multiplier constraints, Zuckerwar and Ash (2006) found that a fluid flow with negligible frictional dissipation could still be affected by quasi-reversible non-equilibrium processes. The research described in this dissertation has explored subtle aspects of those implications. In order to do this, it is necessary to recast the non-equilibrium part of Eq. (2.71) in terms of more-conventional dependent variables.

If $\rho(\xi, P, s)$ is the molar density of a fluid, we can expand it about its equilibrium point:

$$d\rho = \left(\frac{\partial\rho}{\partial\xi}\right)_{P,s} d\xi + \left(\frac{\partial\rho}{\partial P}\right)_{\xi,s} dP + \left(\frac{\partial\rho}{\partial s}\right)_{\xi,P} ds, \quad (2.72)$$

$$\text{so that } \frac{D\rho}{Dt} = \left(\frac{\partial\rho}{\partial\xi}\right)_{P,s} \frac{D\xi}{Dt} + \left(\frac{\partial\rho}{\partial P}\right)_{\xi,s} \frac{DP}{Dt} + \left(\frac{\partial\rho}{\partial s}\right)_{\xi,P} \frac{Ds}{Dt}. \quad (2.73)$$

Using Eq. (2.9) and Eq. (2.10),

$$-\rho\nabla\cdot\mathbf{v} = \left(\frac{\partial\rho}{\partial\xi}\right)_{P,s} \frac{D\xi}{Dt} + \left(\frac{\partial\rho}{\partial P}\right)_{\xi,s} \frac{DP}{Dt}. \quad (2.74)$$

Therefore, we can write:

$$\frac{D\xi}{Dt} = \frac{-\rho \left[\nabla\cdot\mathbf{v} + \frac{1}{\rho} \left(\frac{\partial\rho}{\partial P}\right)_{\xi,s} \frac{DP}{Dt} \right]}{\left(\frac{\partial\rho}{\partial\xi}\right)_{P,s}}. \quad (2.75)$$

From acoustics, the high-frequency adiabatic compressibility is defined

$$\kappa_s^\infty = \frac{1}{\rho} \left(\frac{\partial \rho}{\partial P} \right)_{\xi, s}. \quad (2.76)$$

Utilizing this definition, Eq. (2.75) becomes:

$$\frac{D\xi}{Dt} = -\frac{\rho}{\left(\frac{\partial \rho}{\partial \xi} \right)_{p, s}} \nabla \cdot \mathbf{v} - \frac{\rho \kappa_s^\infty}{\left(\frac{\partial \rho}{\partial \xi} \right)_{p, s}} \frac{DP}{Dt}. \quad (2.77)$$

Consequently, Eq. (2.70) can be written:

$$\rho \frac{D\mathbf{v}}{Dt} = -\rho \nabla \Omega - \nabla P + \rho \alpha \nabla \left[\frac{-\rho}{\left(\frac{\partial \rho}{\partial \xi} \right)_{p, s}} \nabla \cdot \mathbf{v} + \frac{-\rho \kappa_s^\infty}{\left(\frac{\partial \rho}{\partial \xi} \right)_{p, s}} \frac{DP}{Dt} \right]. \quad (2.78)$$

Zuckerwar & Ash, (2006), defined characteristic volumetric and pressure relaxation times:

$$\tau_v = \frac{-\rho}{\left(\frac{\partial \rho}{\partial \xi} \right)_{p, s}}, \tau_p = \frac{-\rho \kappa_s^\infty}{\left(\frac{\partial \rho}{\partial \xi} \right)_{p, s}}. \quad (2.79)$$

Then, Eq. (2.78) could be written in the more compact form:

$$\rho \frac{D\mathbf{v}}{Dt} = -\rho \nabla \Omega - \nabla P + \rho \alpha \nabla \left(\tau_v \nabla \cdot \mathbf{v} + \tau_p \frac{DP}{Dt} \right). \quad (2.80)$$

If these relaxation times (τ_v and τ_p) can be modeled as constants, then,

$$\rho \frac{D\mathbf{v}}{Dt} = -\rho \nabla \Omega - \nabla P + \rho \alpha \tau_v \nabla (\nabla \cdot \mathbf{v}) + \rho \alpha \tau_p \nabla \frac{DP}{Dt}. \quad (2.81)$$

Since the divergence of the velocity vector can be related directly to the material rate of change of density using the conservation of mass, Eq. (2.81) can be interpreted as containing a pair of non-equilibrium terms involving gradients of the material rates of change of density and pressure. The two non-equilibrium terms are scaled with a volumetric relaxation time and a pressure relaxation time, along with the Lagrangian constraint parameter. When dissipative viscous effects are introduced into the equations of motion, we observe that the non-equilibrium “density term” as written in Eq. (2.81), has the same form as the bulk viscous term describing a Newtonian fluid. Hence, the Hamilton’s Principal route for deriving the equations of motion for a flow that is capable of non-equilibrium behavior has resulted in a volumetric relaxation affect that has the same form as bulk viscous dissipation along with a pressure relaxation affect that was not anticipated.

Since $\rho \alpha \tau_v$ represents the same type of parameter as traditional volume viscosity, an overall volume viscous parameter given by $\eta_v = \rho \alpha \tau_v$ can be introduced, and, similarly, a pressure relaxation coefficient, $\eta_p = \rho \alpha \tau_p$, can be defined so that the vector form of the conservation of linear momentum can be written:

$$\rho \frac{D\mathbf{v}}{Dt} = -\rho \nabla \Omega - \nabla P + \eta_v \nabla (\nabla \cdot \mathbf{v}) + \eta_p \nabla \frac{DP}{Dt}. \quad (2.82)$$

Introducing the dissipative viscous terms for a Newtonian fluid results in a governing conservation of momentum equation similar to the Navier Stokes’ Equation:

$$\rho \frac{D\mathbf{v}}{Dt} = -\nabla P + \eta_p \nabla \frac{DP}{Dt} - \rho \nabla \Omega + \left(\eta_v + \frac{4}{3} \mu \right) \nabla (\nabla \cdot \mathbf{v}) - \mu \nabla \times (\nabla \times \mathbf{v}). \quad (2.83)$$

2.1.3 Incompressible flow simplifications

In the absence of body forces and using the Einstein summation convention, Eq.(2.83) can be simplified for incompressible flows, with an allowance for sound production by retaining the terms in braces below:

$$\rho \frac{Dv_i}{Dt} = -\frac{\partial P}{\partial x_i} + \eta_p \frac{D}{Dt} \frac{\partial P}{\partial x_i} + \mu \frac{\partial^2 v_i}{\partial x_i^2} + \eta_p \left[\frac{\partial v_k}{\partial x_i} \frac{\partial P}{\partial x_k} - \frac{(\eta_v + 1/3 \mu)}{\eta_p} \frac{\partial}{\partial x_i} \left(\frac{1}{\rho} \frac{D\rho}{Dt} \right) \right]. \quad (2.84)$$

Using the definitions for η_v and η_p , it has been possible to demonstrate that to very good accuracy, (Ash, Zardadkhan, & Zuckerwar, 2011),

$$a_o^2 = \frac{\eta_v + 1/3 \mu}{\eta_p}. \quad (2.85)$$

It is therefore logical to suppose that the last (braced) term in Eq. (2.84) is a type of acoustic shunt, where

$$\frac{\partial v_k}{\partial x_i} \frac{\partial P}{\partial x_k} = a_o^2 \frac{\partial}{\partial x_i} \left(\frac{1}{\rho} \frac{D\rho}{Dt} \right). \quad (2.86)$$

Consequently, Eq. (2.84) can be simplified to:

$$\rho \frac{Dv_i}{Dt} = -\frac{\partial P}{\partial x_i} + \eta_p \frac{D}{Dt} \frac{\partial P}{\partial x_i} + \mu \frac{\partial^2 v_i}{\partial x_i^2}. \quad (2.87)$$

The vector form of this equation can be written:

$$\rho \frac{D\mathbf{v}}{Dt} = -\nabla P + \eta_p \frac{D}{Dt} \nabla P + \mu \nabla^2 \mathbf{v}. \quad (2.88)$$

2.2 Summary

In this chapter, the governing equations for fluid flows utilizing Hamilton's Principle of Least Action, along with Lagrange multiplier-based constraints, have been derived. The resulting equations resemble the traditional Navier Stokes' equations for incompressible fluid flow with the exception of a term that allows for the departure of pressure from its thermodynamic equilibrium state.

CHAPTER 3

THE STRUCTURE OF AN AXIAL VORTEX

This chapter will examine the influence of pressure relaxation on a two-dimensional axisymmetric axial vortex.

3.1 Introduction

For short periods of time, natural vortical flows like aircraft wake vortices, tornadoes and dust-devils resemble steady line vortices. When the standard Navier Stokes equations are employed, it is not possible to obtain a steady-state, axial vortex solution that is valid over the entire domain for a steady line vortex. The Lamb-Oseen vortex (Lamb, 1932) is a model used to describe a line vortex, but it is an unsteady solution and dissipates rapidly with time. A direct solution of the Navier Stokes equation results either in a rigid rotating column or a potential vortex that decays as $1/r$. This type of model can predict the far-field flow behavior of a vortex but the model cannot predict the flow structure in close proximity of the vortex rotational axis.

In the late nineteenth century, Rankine had already recognized that it was impossible to model the core of a vortex filament using only a potential flow model (Rankine, 1869). He assumed that the inner core behaved like a rigid core and at some distance, the rigidly-rotating core velocity was matched with an outer potential vortex velocity distribution to obtain a continuous velocity solution. However, Rankine's velocity distribution was incompatible with viscous fluid behavior due to the discontinuity in the slope of the velocity distribution.

The exact solution to the Navier Stokes equations proposed by Oseen and Lamb treated the flow as an initial-value, vorticity diffusion problem. A potential flow vortex was assumed to be subjected suddenly to a viscous, zero-velocity centerline. Subsequent experimental comparisons by Gavindaraju & Saffman, (1971) illuminated inconsistencies between the Lamb-Oseen vortex model and experimental axial vortex measurements.

When the non-equilibrium pressure terms were introduced in the Navier-Stokes equations, it was possible to find a steady-state axial vortex velocity distribution that is valid and continuous throughout the flow domain; that recent development (Ash, Zardadkhan and Zuckerwar, 2011) follows.

3.2 The Governing Equations

The governing equations for incompressible flow with pressure relaxation, partitioned with respect to the approximation for sound generation were derived in the previous chapter. In vector form, Eq. (2.88) can be written:

$$\rho \frac{D\mathbf{v}}{Dt} = -\nabla P + \eta_p \frac{D}{Dt} \nabla P + \mu \nabla^2 \mathbf{v}. \quad (3.1)$$

In order to examine an axial vortex, it is convenient to write the vector components of that equation in cylindrical coordinates. The resulting equations are nearly the same as the standard Navier Stokes equations with the exception of the pressure relaxation term $\eta_p \frac{D}{Dt} \nabla P$. The standard form of the continuity equation for steady incompressible flow in cylindrical coordinates is given by:

$$\frac{1}{r} \frac{\partial}{\partial r} (rv_r) + \frac{1}{r} \frac{\partial v_\theta}{\partial \theta} + \frac{\partial v_z}{\partial z} = 0. \quad (3.2)$$

For steady, axisymmetric incompressible flow, the radial component of the conservation of momentum equation is then given by:

$$v_r \frac{\partial v_r}{\partial r} - \frac{v_\theta^2}{r} + v_z \frac{\partial v_r}{\partial z} = v \left(\frac{\partial^2 v_r}{\partial r^2} + \frac{1}{r} \frac{\partial v_r}{\partial r} - \frac{v_r}{r^2} + \frac{\partial^2 v_r}{\partial z^2} \right) + \frac{\eta_p}{\rho} \left[v_r \frac{\partial^2 P}{\partial r^2} + v_z \frac{\partial^2 P}{\partial z \partial r} \right] - \frac{1}{\rho} \frac{\partial P}{\partial r}, \quad (3.3)$$

the azimuthal component is:

$$v_r \frac{\partial v_\theta}{\partial r} + \frac{v_r v_\theta}{r} + v_z \frac{\partial v_\theta}{\partial z} = v \left(\frac{\partial^2 v_\theta}{\partial r^2} + \frac{1}{r} \frac{\partial v_\theta}{\partial r} - \frac{v_\theta}{r^2} + \frac{\partial^2 v_\theta}{\partial z^2} \right) + \frac{\eta_p}{\rho} \left[\frac{v_\theta}{r} \left(\frac{\partial P}{\partial r} \right) \right], \quad (3.4)$$

and the corresponding axial component is:

$$v_r \frac{\partial v_z}{\partial r} + v_z \frac{\partial v_z}{\partial z} = v \left\{ \frac{\partial^2 v_z}{\partial r^2} + \frac{1}{r} \frac{\partial v_z}{\partial r} + \frac{\partial^2 v_z}{\partial z^2} \right\} + \frac{\eta_p}{\rho} \left[v_r \frac{\partial^2 P}{\partial r \partial z} + v_z \frac{\partial^2 P}{\partial z^2} \right] - \frac{1}{\rho} \frac{\partial P}{\partial z}. \quad (3.5)$$

For flows with no axial or radial velocity components, the continuity equation is satisfied trivially. Neglecting any axial flow, the axial component of the conservation of momentum equation is not required. The radial component reduces to:

$$\rho \frac{v_\theta^2}{r} = \frac{\partial P}{\partial r}, \quad (3.6)$$

exhibiting no direct influences due to pressure relaxation. However, the azimuthal component of the conservation of momentum equation:

$$0 = \mu \left(\frac{\partial^2 v_\theta}{\partial r^2} + \frac{1}{r} \frac{\partial v_\theta}{\partial r} - \frac{v_\theta}{r^2} \right) + \eta_p \left[\frac{v_\theta}{r} \left(\frac{\partial P}{\partial r} \right) \right], \quad (3.7)$$

includes a cross-coupling between the swirl velocity and the radial pressure gradient. In the absence of pressure relaxation, the radial component of the conservation of momentum equations is trivial; however, with the included pressure relaxation term, the radial pressure gradient expression, Eq. (3.6), can be substituted into Eq (3.7) to get:

$$\rho\eta_p \frac{v_\theta^3}{r^2} + \mu \left(\frac{\partial^2 v_\theta}{\partial r^2} + \frac{1}{r} \frac{\partial v_\theta}{\partial r} - \frac{v_\theta}{r^2} \right) = 0. \quad (3.8)$$

The resulting equation (3.8) is a non-linear ordinary differential equation. That ordinary differential equation can be solved for the case of an axial line vortex. Since the centerline swirl velocity must be zero, and the far-field swirl velocity should converge to a prescribed circulation potential vortex, the following boundary conditions can be utilized:

$$\lim_{r \rightarrow 0} v_\theta(r) \rightarrow 0, \quad \lim_{r \rightarrow \infty} v_\theta(r) \rightarrow \frac{\Gamma_0}{2\pi r}. \quad (3.9)$$

Making use of the kinematic viscosity, pressure relaxation coefficient and a specified circulation, the following dimensionless variables can be formed:

$$r = \sqrt{\nu\eta_p} \bar{r}, \quad v_\theta = \frac{\Gamma_0}{2\pi\sqrt{\nu\eta_p}} u(\bar{r}). \quad (3.10)$$

Thus, the dimensionless governing equation can be written:

$$\bar{r}^2 \frac{\partial^2 u}{\partial \bar{r}^2} + \bar{r} \frac{\partial u}{\partial \bar{r}} - u + R_\Gamma^2 u^3 = 0, \quad (3.11)$$

where R_Γ is the circulation-based Reynolds number defined as:

$$R_\Gamma = \frac{\Gamma_0}{2\pi\nu},$$

and the transformed boundary conditions are:

$$\left\langle \lim_{\bar{r} \rightarrow 0} u(\bar{r}) \rightarrow 0, \quad \lim_{\bar{r} \rightarrow \infty} u(\bar{r}) \rightarrow 1 \right\rangle. \quad (3.12)$$

3.3 Steady-State Solution

In order to solve the non-linear ordinary differential equation, it is often convenient to introduce the following dimensionless independent variable, ζ , and an associated scaling parameter, k , given by:

$$\zeta = \sqrt{\frac{R_\Gamma^2 - 2}{2}} \ln \bar{r}, \quad k = \sqrt{\frac{R_\Gamma^2}{2 - R_\Gamma^2}} \quad (R_\Gamma^2 \neq 2). \quad (3.13)$$

Upon substituting these expressions into Eq. (3.11), the resulting transformed equation becomes:

$$\frac{d^2 u}{d\zeta^2} = -(1 + k^2)u + 2k^2 u^3. \quad (3.14)$$

This is a well-known standard elliptic differential equation whose solution is the Jacobi elliptic sn function. This solution, however, is not appropriate for satisfying the boundary conditions for an axial vortex.

Alternatively, a simpler solution to Eq. (3.11) exists in the following form:

$$u(\bar{r}) = \frac{8\bar{r}}{8\bar{r}^2 + R_\Gamma^2}. \quad (3.15)$$

Using that expression, the resulting dimensionless velocity depends only on the circulation-based Reynolds number. If the vortex core radius is defined as the radial distance where the swirl velocity is maximum, the core radius can be obtained by taking the first derivative of the swirl velocity and equating it to zero. That is,

$$\frac{du}{dr}(r_{core}) = 0, \quad (3.16)$$

this requires that

$$\frac{8}{8\bar{r}_{core}^2 + R_\Gamma^2} - \frac{128\bar{r}^2}{(8\bar{r}^2 + R_\Gamma^2)^2} = 0, \quad (3.17)$$

and consequently the dimensionless core radius is given by

$$\bar{r}_{core} = \frac{R_\Gamma}{\sqrt{8}}. \quad (3.18)$$

By substituting Eq. (3.18) into Eq. (3.15), the corresponding dimensionless maximum swirl velocity can be written:

$$u_{max} = \frac{\sqrt{2}}{R_\Gamma}. \quad (3.19)$$

Definitions (3.10) can be utilized in the dimensionless solution, Eq. (3.13), to obtain the dimensional forms of the core radius and the maximum swirl velocity:

$$r_{core} = \frac{\Gamma_0}{4\pi} \sqrt{\frac{\eta_p}{2\nu}}, \quad (3.20)$$

and

$$v_{\theta, \max} = \sqrt{\frac{2\nu}{\eta_p}}. \quad (3.21)$$

3.3.1 Properties of the Steady-State Axial Vortex Solution

Converting dimensionless Eq. (3.15) to its dimensional form permits the swirl velocity to be represented in terms of the core radius and the maximum swirl velocity, i.e.

$$v_{\theta}(r) = 2v_{\theta, \max} \frac{(r/r_{core})}{(r/r_{core})^2 + 1}. \quad (3.22)$$

In the absence of pressure relaxation, Eq. (3.20) shows that the core radius will be zero and the maximum centerline velocity will be infinite, indicating that a potential flow vortex solution results from satisfying the radial component of the Navier Stokes equation when the azimuthal velocity varies only with radius. For very large values of the pressure relaxation coefficient, the inner core of the vortex tends to behave like a rigid-body rotation.

The size of the vortex core is related linearly to the magnitude of the circulation. On the other hand, the maximum swirl velocity does not depend on circulation; rather, it is a function of the pressure relaxation coefficient and the viscosity.

The steady state solution Eq (3.22) is functionally the same equation that was proposed originally by Burnham & Hallock (1982) using empirical fitting of experimental data for aircraft trailing line vortices.

3.3.2 The Pressure Distribution

Using the velocity distribution for an axial vortex, given by Eq. (3.22), it is now possible to employ the radial component of the conservation of momentum equation, Eq. (3.6), to determine the pressure distribution for an axial vortex in a constant-density fluid. Assuming that the far-field pressure is specified as P_∞ , Eq. (3.6) can be integrated to write

$$P_\infty - P(r) = \int_r^\infty \rho \frac{v_\theta^2}{r} dr = 4 \frac{\mu}{\eta_p} \frac{1}{(r/r_{core})^2 + 1}. \quad (3.23)$$

The radial pressure distribution is then given by

$$P(r) = P_\infty - 4 \frac{\mu}{\eta_p} \frac{1}{(r/r_{core})^2 + 1}. \quad (3.24)$$

3.3.3 The Circulation

The Burnham & Hallock (1982) model suggested that the circulation at the core of an axial trailing line vortex was one half the far-field circulation. Govindaraju & Saffman (1971) have determined that neither the diffusing Lamb vortex, nor the Rayleigh vortex model predict the circulation in the region around the vortex core correctly. Their compilation of experimental observations indicated that the ratio between the circulation at the vortex core radius and the far-field circulation value ranged between 0.4 and 0.6.

The circulation for a line vortex at any radius is given by:

$$\Gamma(r) = 2\pi r v_\theta(r). \quad (3.25)$$

Using the velocity distribution given by Eq. (3.22), the circulation distribution for this line vortex can be written:

$$\Gamma(r) = 4\pi r v_{\theta, \max} \frac{(r/r_{core})}{(r/r_{core})^2 + 1}. \quad (3.26)$$

Consequently, the circulation in terms of the far-field circulation, Γ_0 , is given by:

$$\frac{\Gamma(r)}{\Gamma_0} = \frac{(r/r_{core})}{(r/r_{core})^2 + 1}. \quad (3.27)$$

The circulation at the core radius can then be written:

$$\frac{\Gamma(r_{core})}{\Gamma_0} = \frac{1}{2} \Rightarrow \Gamma(r_{core}) = \frac{1}{2} \Gamma_0. \quad (3.28)$$

The value of circulation predicted by relationships (3.27) and (3.28) are within the range of observed experimental values compiled by Govindaraju & Saffman (1971) and their data covered a wide range of circulation-based Reynolds numbers.

3.4 Validation of the Predicted Profiles

The velocity distribution and associated circulation relationships agree with the empirically-based relationships that have been developed earlier by others, e.g. (Burnham & Hallock, 1982). It is appropriate now to compare the theoretically-based relationships with experimentally observed data.

3.4.1 Velocity Profile

The agreement between the velocity profile given by Eq. (3.22) with the existing empirical correlation data characterizing aircraft trailing vortices has already been noted.

Figure 3.1 represents a comparison of the predicted velocity profile with reported velocity measurements for actual aircraft flight experiments by McCormick, Tangler & Sherrie (1968), wind tunnel measurements by McAlister & Takahashi (1991) and towing tank experiments in water by Valdhius, Scarano & Van (2003) and Baker et. al (1974). Figure 3.2 represents experimentally-measured turbulent tangential velocities within a dust devil recorded by Sinclair, (1969). Those data were collected utilizing an instrumented tower on a vehicle that was driven deliberately to a position located in the anticipated center of a dust devil path and parked.

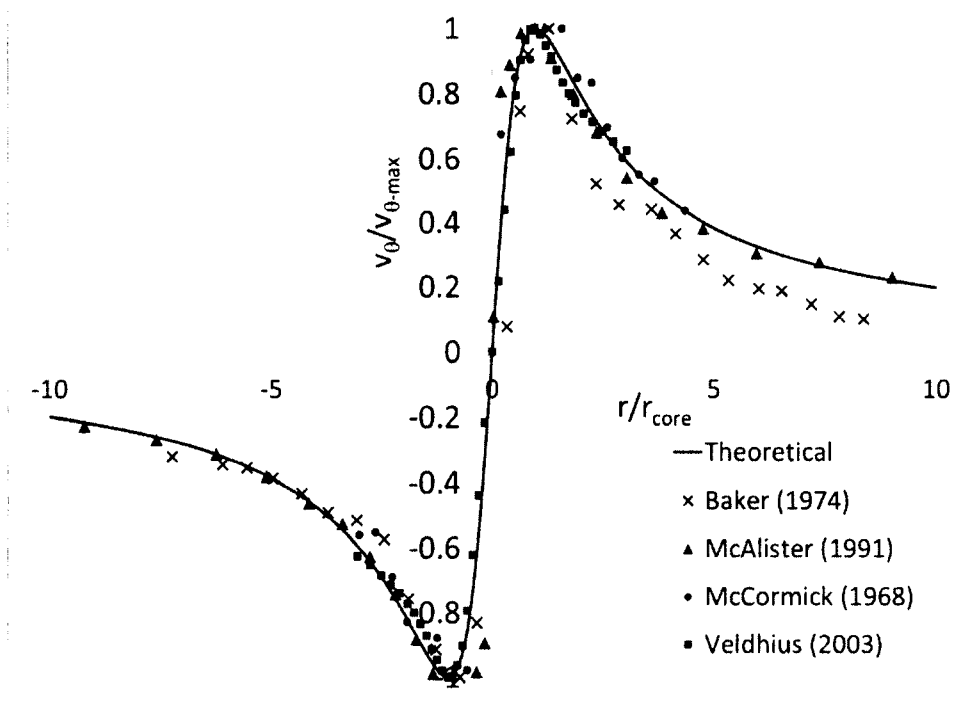


Figure 3.1 Velocity distribution for a vortex filament

Unlike aircraft wake vortex data where neither pressure deficits nor local ambient temperatures and humidity levels were measured, Sinclair (1969) measured ambient temperature, velocity and pressure deficit distributions in three dust devils.

Unfortunately, the relative humidity was not measured, but since the elevation of the desert location where Sinclair made his measurements is known to reasonable accuracy and the diurnal variations in humidity levels observed in nearby desert locations (near Tucson, AZ) are repetitive, the probable humidity levels that existed during Sinclair's observations can be estimated. Although quite warm, ambient temperatures were relatively constant for the three dust devils studied, enabling the use of a theoretically-predicted pressure relaxation coefficient that was nearly constant for the warm, dry air.

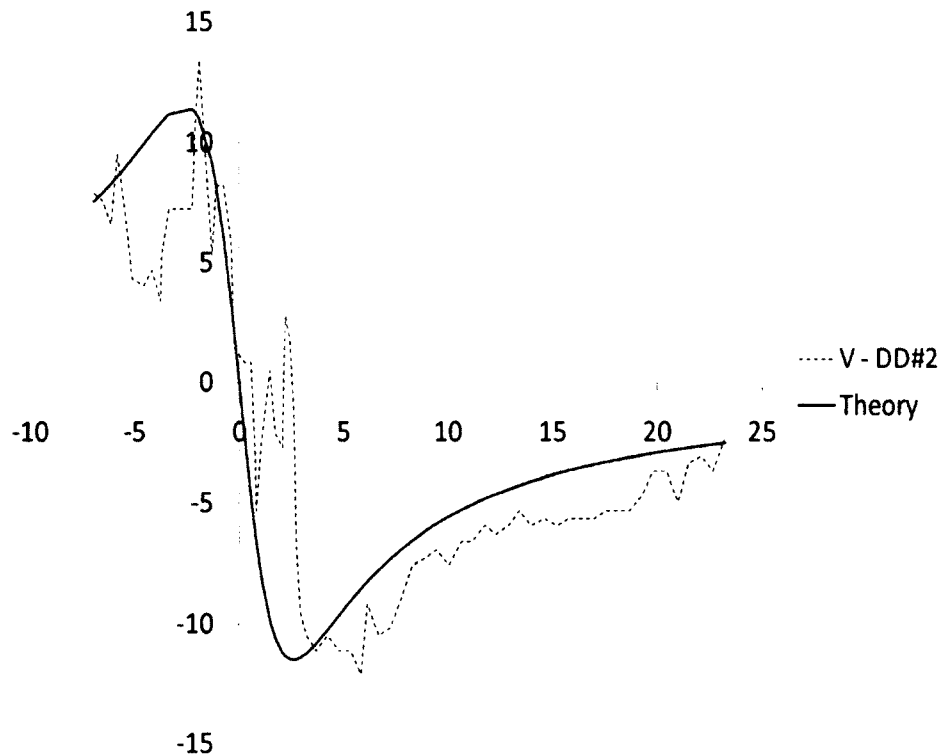


Figure 3.2 Comparison of theoretical velocity profile with Sinclair Dust Devil # 2

3.4.2 Pressure Profiles

Utilization of the incompressible Bernoulli equation to predict the pressure deficit at the centerline of an axial vortex suggests that the centerline pressure should return to

the far field pressure since the centerline velocity must be zero. However, the current theory predicts that non-equilibrium pressures within this type of axial vortex continue to decrease within the core until reaching a maximum pressure deficit on the centerline of the vortex. The present theory is supported by the experimental observations made in dust devils and tornadoes.

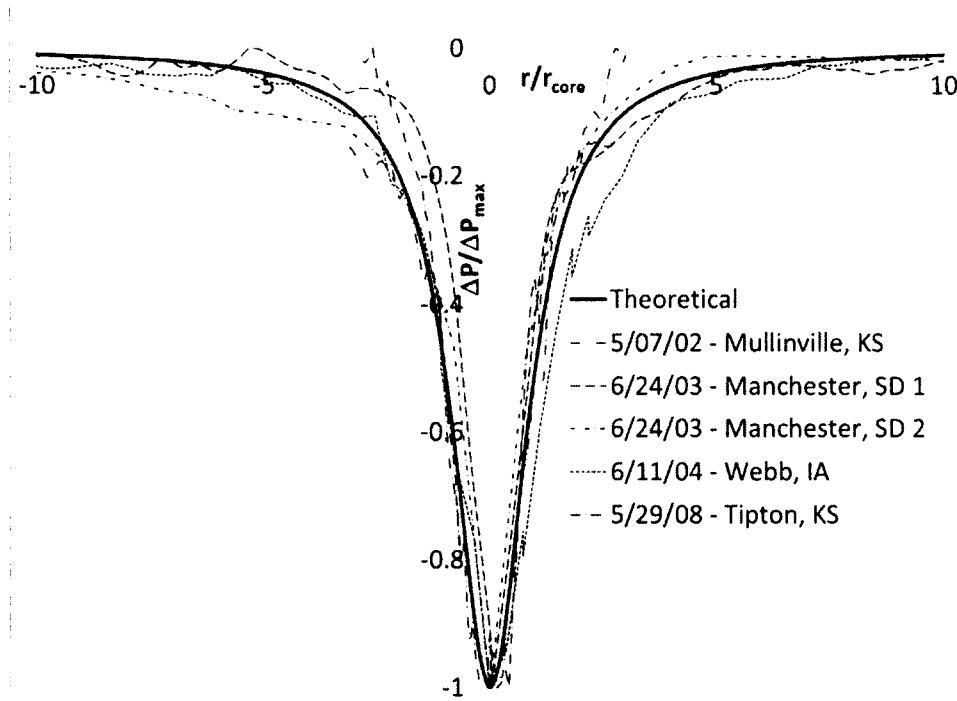


Figure 3.3 Comparison of the normalized tornado pressure profile with the theoretical pressure profile.

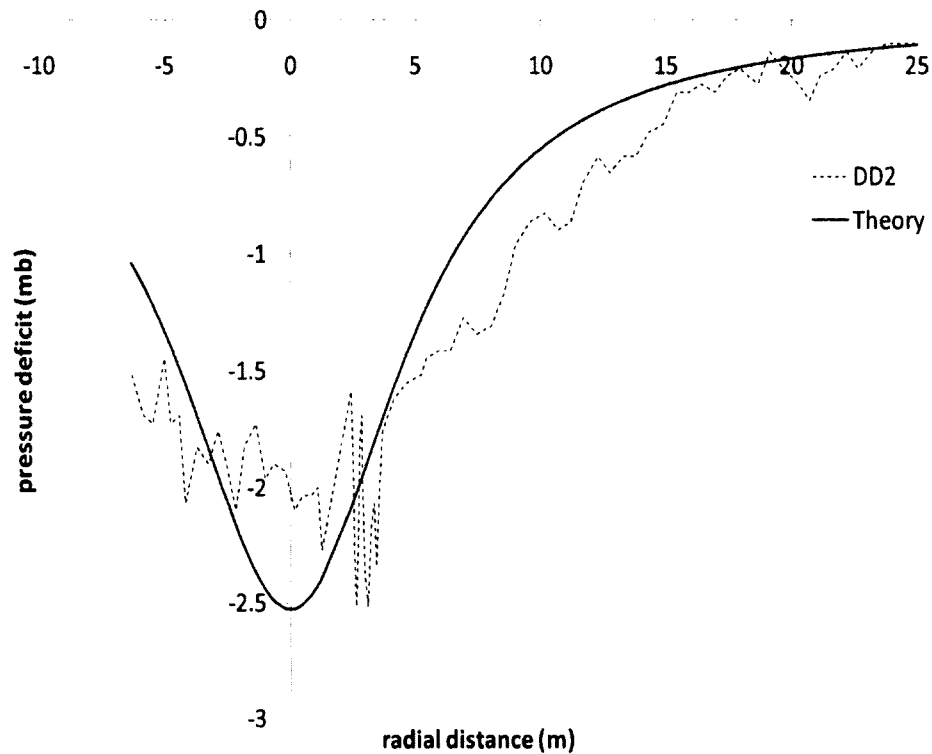


Figure 3.4 Comparison of dust devil profile with the theoretical pressure profile.

3.4.3 Prediction of the Pressure Relaxation Coefficient using Pressure Deficit

Equation (3.25) can be employed to determine the centerline pressure deficit. The centerline pressure, P_0 , is thus given by,

$$P_0 = P_\infty - 4 \frac{\mu}{\eta_p}. \quad (3.30)$$

Since the centerline pressure deficit depends only on the dynamic viscosity and the pressure relaxation coefficient, it is possible to relate the pressure relaxation coefficient directly to the measured maximum pressure deficit *for a steady-state, laminar axial*

vortex. That is, the pressure relaxation coefficient, η_p , can be expressed in terms of the measured pressure deficit and the tabulated dynamic viscosity according to the formula,

$$\eta_p = \frac{4\mu}{P_\infty - P_0}. \quad (3.31)$$

Equation (3.31) is a useful relationship for determination of the pressure relaxation coefficient in tornadoes or dust devils, based only on the pressure deficit and the dynamic viscosity of air. However, since those axial vortices are known to be turbulent, it is necessary to replace the dynamic viscosity represented in eq. (3.31) with an effective turbulent viscosity which can be substantially larger than the fluid mechanical viscosity. The turbulent version of Eq. (3.31) can be written:

$$\eta_p = \frac{4\rho v_{Turb}}{P_\infty - P_0}. \quad (3.32)$$

Table 3.1 provides a comparison between the estimated pressure relaxation coefficient and the calculated pressure relaxation coefficient using the available weather data for the tower fly-by experiments reported by Garodz & Clawson (1969).

Table 3.1 Estimation of Pressure Relaxation Coefficient using Aircraft Experiments

Experiment	R_Γ	r_{core}, m	$v, m^2/s$	$\eta_p, \mu s$ Estimated	Ambient Conditions	$\eta_p, \mu s$ Calculated
NOAA B-757	380,500	0.061	16.96×10^{-6}	0.0121	9°C 74% R.H	0.5
NOAA B-757	330,200	0.274	17.07×10^{-6}	0.323	10.5°C 52% R.H	0.72
NOAA B-767	356,800	0.091	16.71×10^{-6}	0.0311	7.0°C 51% R.H.	0.84
NOAA B-767	381,500	0.244	18.16×10^{-6}	0.180	21°C 18% R.H.	7.0

It can be seen that the estimated values of pressure relaxation coefficient are an order of magnitude smaller than the calculated values. This discrepancy is believed to be due mainly to the fact that the tabulated values of kinematic viscosity were used to estimate the values of the pressure relaxation coefficient but in practice, the vortices were turbulent and thus the effective turbulent viscosity should be used to estimate these values.

3.5 Summary

Analytical expressions for the velocity, circulation and pressure distributions describing an incompressible axisymmetric axial vortex with non-equilibrium pressure have been developed. The predicted distributions were then compared with various experiments reported in the literature and representing a variety of physical conditions that spanned a large range of circulation-based Reynolds numbers. The comparisons

between the current theory and the range of experiments have shown good agreement between the results.

CHAPTER 4

RIGIDLY ROTATING FLUID COLUMN NEAR THE GROUND

In Chapter 2, the equations governing fluid flow, including pressure relaxation effects, were derived and then in Chapter 3 the influence of pressure relaxation on an axisymmetric axial vortex filament was examined. In this chapter, three-dimensional steady flows with radial and axial velocity components interacting with a solid ground plane will be studied.

4.1 Introduction

In the absence of a solid boundary, a rotating fluid column has characteristics that are similar to the line vortex core region studied in the previous chapter. This type of flow can represent important features of certain meteorological systems like the central regions of tornadoes, dust devils and hurricanes.

4.2 Mathematical Model

The inner core of geophysical vortices like dust devils and tornadoes can be modeled as an idealized, nearly rigid column of fluid rotating above a solid plane. The simple similarity model developed by Boedewadt (1940) was discussed in Chapter 1, and represents the starting point for the present study. Boedewadt assumed a nearly rigid column of fluid was rotating over a stationary ground plane boundary layer. Schlichting (1968) has discussed this solution in some detail, and Figure 4.1 provides a physical interpretation of this type of flow. Employing an axisymmetric Navier-Stokes equation

model, Boedewadt made use of the following similarity variable and associated transformations.

$$\eta = z\sqrt{\frac{\omega}{\nu}}, \quad v_r = r\omega F(\eta), \quad v_\theta = r\omega G(\eta), \quad v_z = \sqrt{\nu\omega}H(\eta),$$

$$\frac{1}{\rho} \frac{\partial p}{\partial r} = r\omega^2, \quad (4.1)$$

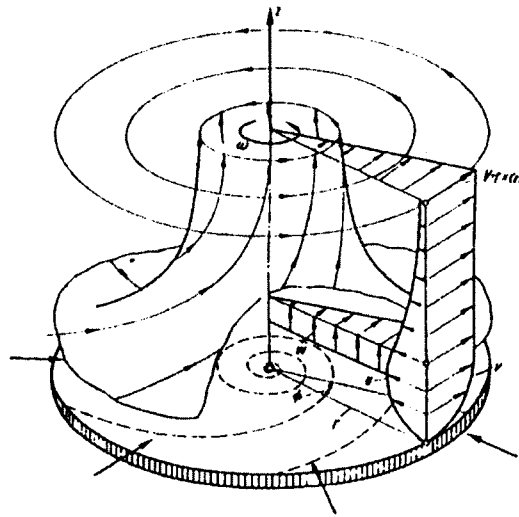


Figure 4.1 A physical representation of flow rotating near the ground (Schlichting, 1968)

In the present case, the steady state, axisymmetric form of the Navier Stokes equations incorporating pressure relaxation, as represented by Eq. (2.88), can be written

$$v_r \frac{\partial v_r}{\partial r} - \frac{v_\theta^2}{r} + v_z \frac{\partial v_r}{\partial z} = \nu \left(\frac{\partial^2 v_r}{\partial r^2} + \frac{1}{r} \frac{\partial v_r}{\partial r} - \frac{v_r}{r^2} + \frac{\partial^2 v_r}{\partial z^2} \right) +$$

$$+ \frac{\eta_\rho}{\rho} \left[v_r \frac{\partial^2 P}{\partial r^2} + v_z \frac{\partial^2 P}{\partial z \partial r} \right] - \frac{1}{\rho} \frac{\partial P}{\partial r}, \quad (4.2)$$

$$v_r \frac{\partial v_\theta}{\partial r} + \frac{v_r v_\theta}{r} + v_z \frac{\partial v_\theta}{\partial z} = v \left(\frac{\partial^2 v_\theta}{\partial r^2} + \frac{1}{r} \frac{\partial v_\theta}{\partial r} - \frac{v_\theta}{r^2} + \frac{\partial^2 v_\theta}{\partial z^2} \right) + \frac{\eta_p}{\rho} \left[\frac{v_\theta}{r} \left(\frac{\partial P}{\partial r} \right) \right], \quad (4.3)$$

$$v_r \frac{\partial v_z}{\partial r} + v_z \frac{\partial v_z}{\partial z} = v \left\{ \frac{\partial^2 v_z}{\partial r^2} + \frac{1}{r} \frac{\partial v_z}{\partial r} + \frac{\partial^2 v_z}{\partial z^2} \right\} + \frac{\eta_p}{\rho} \left[v_r \frac{\partial^2 P}{\partial r \partial z} + v_z \frac{\partial^2 P}{\partial z^2} \right] - \frac{1}{\rho} \frac{\partial P}{\partial z}. \quad (4.4)$$

The axisymmetric continuity equation is given by

$$\frac{\partial v_r}{\partial r} + \frac{v_r}{r} + \frac{\partial v_z}{\partial z} = 0 \quad (4.5)$$

Employing Boedewadt's similarity transformations given in Eq. (4.1), the governing similarity equations, modified to include pressure relaxation, reduce to:

$$(F - \eta_p \omega) F - G^2 + HF' - F'' + 1 = 0 \quad (4.6)$$

$$(2F - \eta_p \omega) G + G' H - G'' = 0 \quad (4.7)$$

$$2F + H' = 0 \quad (4.8)$$

This set of equations is nearly identical with Boedewadt's equations except for a type of rotational offset parameter resulting from the addition of the pressure relaxation terms. It is interesting to note that the parameter that controls the non-equilibrium behavior of these equations is $\eta_p \omega$, which is proportional to the angular velocity. As was mentioned in Chapter 1, a number of authors (Bellamy-Knights, 1974; Hatton, 1975; Raymond & Rao, 1978) have suggested that the stagnation zone at the top of a tornado

vortex column was controlled by a similar parameter, also proportional to the angular rate of rotation

4.2.1 Boundary Conditions

In order to solve this ordinary differential equation set, appropriate boundary conditions are required. The no-slip and no penetration conditions on the ground plane yield the following requirements:

$$F(0) = 0, \quad (4.9)$$

$$G(0) = 0, \quad (4.10)$$

$$\text{and } H(0) = 0. \quad (4.11)$$

Away from the ground plane boundary, the rotating column inner core is expected to behave like a rigid body and the angular velocity of the core must therefore asymptote to a constant value. The azimuthal component of the velocity in the far-field can then be used to obtain the following boundary condition

$$G(\infty) = 1 \quad (4.12)$$

Due to the lack of experimental measurements, it is necessary to infer the remaining far field boundary conditions for the radial and axial components of the similarity functions. When the far-field swirl velocity is assumed to approach a constant, obviously its first and second derivatives must vanish at large distances from the ground plane. Therefore, from the azimuthal component of the conservation of momentum equation, Eq. (4.7) can be employed to obtain the requirement that:

$$2F(\infty) - \eta_r \omega = 0 \quad (4.13)$$

or,

$$F(\infty) = \frac{\eta_r \omega}{2} . \quad (4.14)$$

This boundary condition suggests that there will be radial outflow at large distances from the ground plane boundary. If this boundary condition for the radial similarity function is imposed, the continuity equation (4.8), results in the boundary condition requirement that, in the limit, the slope of the axial similarity function must satisfy

$$\lim_{\eta \rightarrow \infty} \frac{dH}{d\eta} = -\eta_r \omega . \quad (4.15)$$

This implies that in order to sustain a radial outflow, as prescribed by boundary condition (4.14), the overall flow must incorporate a decelerating axial flow component whose axial derivative approaches a constant value. If the slope of the axial similarity function asymptotes to a constant value, it is logical to conclude that at some spatial distance above the ground plane, the axial velocity component must go to zero and then reverse direction. *Inclusion of non-equilibrium pressure effects in a column of rigidly-rotating fluid, bounded from below by a fixed ground plane, produces a spatially-varying axial velocity distribution with a free-standing stagnation plane at the top of the column.* In order for these boundary conditions to be consistent with all of the governing equations, it is also necessary for the similarity functions to satisfy the conservation of radial momentum in the asymptotic limit. That is, when the limiting values of F and H' are imposed, the remaining far field boundary condition is

$$\lim_{\eta \rightarrow \infty} H \frac{dF}{d\eta} = - \left(\frac{\eta_p \omega}{2} \right)^2. \quad (4.16)$$

Since this limiting boundary condition involves a function that increases monotonically, multiplied by the derivative of a function that becomes a constant in the limit (its first derivative goes to zero), it represents a requirement on the numerically-integrated solutions that can only be met *a posteriori*. That requirement will be discussed later in this analysis. The governing equations, Eq. (4.6)-(4.8), with the boundary conditions, (4.9)-(4.15), can be integrated numerically.

The appearance of the stagnation point, implied from Eq. (4.15), results from the inclusion of the pressure relaxation parameter. Pressure relaxation causes the radial component of the flow to turn outward, away from the ground, which in turn causes the axial velocity component to reverse direction at the stagnation point.

Boundary conditions similar to the ones developed here have been suggested by various authors attempting to model a stagnation point in vortices with axial flow (Bellamy-Knights, 1974). While the authors were able to obtain a stagnation point, they did not have a rigorous mathematical foundation for using these boundary conditions. Their solutions could only be applied to unsteady flows because their similarity transformations were functions of time, decaying very rapidly.

If there are no pressure relaxation effects ($\eta_p=0$), then the similarity expressions for the two transformed conservation of momentum equations (4.6) and (4.7) return to the equations that were originally developed by Boedewadt. The appropriate boundary condition for the far field component of the radial component of velocity is zero in that

case, as proposed by Boedewadt. Consequently, in the absence of pressure relaxation, it is not possible to reproduce a stagnation location in the rotating column of fluid.

4.3 Numerical Procedure

Equations (4.6) – (4.8) constitute a set of non-linear ordinary differential equations that can be solved numerically using off-the-shelf software. MATLAB function *bvp4c*, from MathWorks, Inc., was utilized to solve these equations. Their *bvp4c* general solver is designed to solve a large class of boundary value problems governed by ordinary differential equations. The solver utilizes Simpson's method with residual control. It is implemented as an implicit fourth order Runge-Kutta formula and the solutions were obtained at all of the collocation points. The mesh was selected automatically within the required domain, based on a reverse interpolation strategy (Kierzenka & Shampine, 2001). If the resulting solution was not sufficiently smooth and there were jumps in the solution, the mesh in that region was refined until a smooth solution meeting the desired tolerance was achieved. Details of the MATLAB implementation employed in this study are contained in Appendix B. Based on numerous simulation studies, it was determined that the *bvp4c* integration package met the requirements for this study.

4.3.1 Implementation of Far Field Boundary Conditions

As is the case for a variety of two-point boundary value problems spanning an infinite domain, it was necessary to pay special attention to the far field boundary conditions. Numerical experiments were started using a small, one-dimensional domain and the domain was stretched subsequently until the radial and azimuthal components of

the similarity velocity functions were observed to converge toward their expected asymptotic values. Since different types of convergence behavior were expected for the three similarity functions, it was important to demonstrate that a concurrent asymptotic convergence behavior was exhibited in the first derivative of the axial component of the similarity velocity function.

In the absence of pressure relaxation, the three similarity functions and associated boundary conditions were the same as Boedewadt's original solution. Furthermore, the original infinite domain, two-point boundary value problem involved the same boundary conditions. While pressure relaxation coefficients for air can only be predicted theoretically, the theory (Ash, Zardadkhan and Zuckerwar, 2011) suggests that the pressure relaxation coefficient for air is on the order of a microsecond, which means that the scaling parameter ($\eta_p \omega$) can be quite small for most geophysical flows. In order to examine how the introduction of pressure relaxation altered the resulting similarity solutions, an extremely large value ($\eta_p \omega = 0.1$) was selected. That parametric value was considered to be a useful way to examine how the behavior of the similarity functions changed when a strong pressure relaxation influence was present.

The numerical solution procedures were examined by first setting the pressure relaxation parameter ($\eta_p \omega$) equal to zero to make sure that Boedewadt's (1940) solution was duplicated. To the accuracy of the tabulated results, the current numerical techniques produced results that agreed with the earlier work, as shown in Figure 4.2 (Boedewadt's functions are displayed using his original similarity function names).

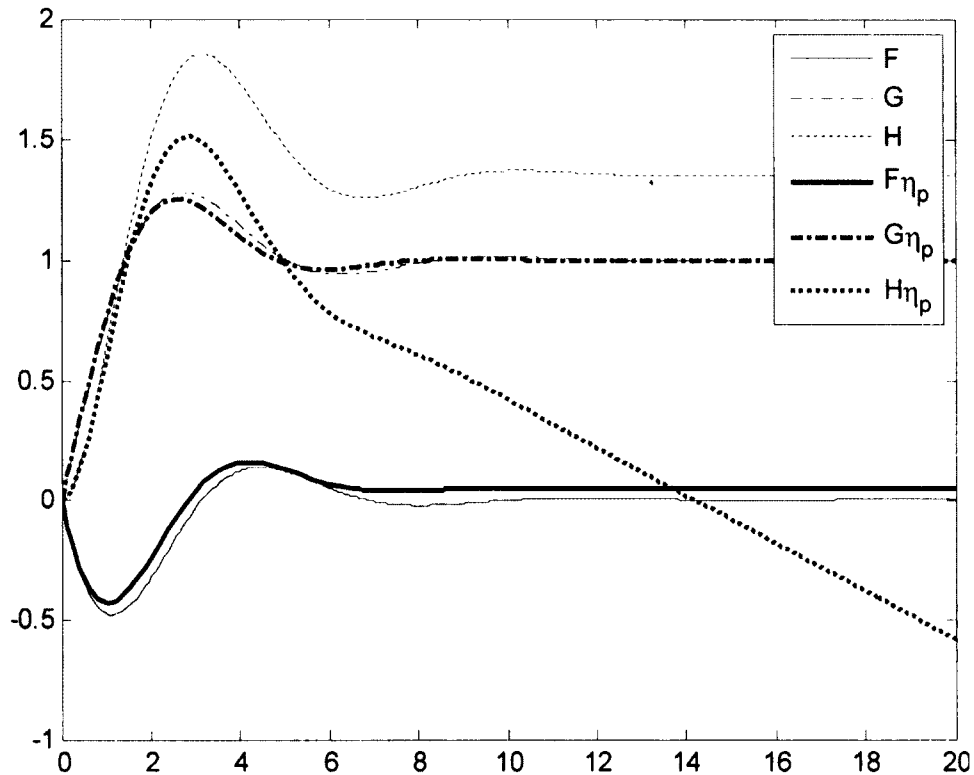


Figure 4.2 Comparison of the similarity solutions with (bolder lines) and without (finer lines) pressure relaxation

Next, the equations were integrated numerically using $\eta_p \omega = 0.1$. Those numerical results are also displayed in Figure 4.2. With the accentuated pressure relaxation parameter, it can be seen that there are only subtle changes in the radial similarity function (F). However, it can be seen that the radial function is indeed approaching a non-zero value of 0.05 asymptotically, as prescribed by the boundary condition. The circumferential similarity function (G) nearly coincides with the original solution and it would therefore be very difficult to discern any differences between the circumferential velocities if pressure relaxation effects were present. However, the axial similarity function, though starting out with a similar shape to the original solution,

quickly diverges and, in compliance with the modified far field boundary condition, asymptotes toward a straight line with a negative slope.

The slope of the axial component depends upon the parameter $\eta_p\omega$. Similar observations with respect to an angular rotation parameter were made by others (Raymond & Rao, 1978). Studies by Hatton (1975) had also shown that the axial velocity profile depended on a parameter that was proportional to the angular velocity. It has been common to assume that Rossby number (R_o) should be used as a parameter for characterizing the flow. The Rossby number is the ratio of the inertial to the Coriolis force. Specifically, that Rossby number was been defined:

$$R_o = V\delta^{-1}\Omega_s^{-1} \quad (4.15)$$

where V is the idealized tangential velocity, observed at the top of the boundary layer, δ is a characteristic depth and Ω_s is the angular velocity of the rotating boundary below. Hence, the smaller the Rossby number, the stronger are the effects of the Coriolis forces. In the absence of turbulence, and for no-slip boundary conditions, Raymond & Rao (1978) have concluded that the Rossby number has to be set to zero and the stagnation point cannot be found. Experimental work (Ward, 1972) has also shown no relationship between Rossby number and the stagnation point.

Although, theoretical studies made by a number of researchers suggest the dependence of the axial and radial velocities on Rossby number, it cannot be used for important geophysical flows like tornadoes, which are over a solid stationary boundary. The angular velocity, Ω_s for such a case will be zero and therefore the Rossby number will be infinite. Turbulent slip velocities have been used to overcome that obstacle for

such cases (Bellamy-Knights, 1974; Hatton, 1975; Raymond & Rao, 1978). With pressure relaxation, the equations do not depend upon modified bottom plane boundary conditions; rather the column height depends on the angular velocity of the fluid column and the pressure relaxation coefficient. The modified equations accommodate the no-slip boundary conditions on the ground while exhibiting the stagnation plane that is observed in physical flows.

Based on the numerical tests performed in this study, it was apparent that the minimum dimensionless distance where the similarity functions closely approximated their limiting asymptotic boundary conditions varied with the magnitude of the pressure relaxation parameter. Higher values of the pressure relaxation parameter resulted in lower nominal stagnation distances. A lower value of pressure relaxation coefficient corresponds with a higher stagnation elevation. As mentioned, previously, Zuckerwar and Ash (2009) have predicted the dependence of the pressure relaxation coefficients in air on the relative humidity, indicating that higher relative humidities result in smaller pressure relaxation coefficients. This theoretical observation is justified by physical flows like dust devils and tornadoes. Tornadoes are known to have much higher moisture content (lower pressure relaxation coefficients) than dust devils. Thus, the height of the funnel-like stagnation top of a dust devil is usually much lower than the stagnation top of a tornado which can rise all the way up into the clouds.

4.4 The pressure distribution

If the flow is assumed to be axisymmetric, the pressure distribution can be assumed to be:

$$p = p_x(x) + p_z(z). \quad (4.16)$$

Using the radial pressure gradient described in Eq. (4.1),

$$p = \frac{\rho(r\omega)^2}{2} + p_z(z) + c \quad (4.17)$$

The variation of the pressure with height is given by:

$$p_z = -\rho gz + p_o \quad (4.18)$$

Then, the pressure distribution within the column is given by:

$$p = \frac{\rho(r\omega)^2}{2} - \rho gz + p_o, \quad (4.19)$$

where, p_o is the pressure in the center of the vortex on the ground level. This pressure distribution is valid only within the core of the rotating column.

CHAPTER 5

ROTATING FLUID COLUMN – RESULTS AND DISCUSSION

In this chapter, the results for an axisymmetric, rotating flow above a solid plane, including pressure relaxation, are presented. The values of $\eta_p \omega$ chosen for the numerical results shown in the figures ranges from 0.001 to 0.1. Although some of the values of the parameter are relatively high for actual physical flows, they were selected to demonstrate the effect of this parameter in establishing the stagnation plane. Smaller values of $\eta_p \omega$ will also produce stagnation planes, but the stagnation zone extends the computational domain to excessively large distances.

5.1 The Velocity Distribution

In order to obtain the velocity profiles, the numerical experiments were run employing values of the parameter $\eta_p \omega$ as 0.0 (corresponding to the Boedewadt (1940) solution), 0.001, 0.01 and 0.1. Figure 5.1 illuminates the degree to which non-equilibrium pressure, via the pressure relaxation coefficient, affects this rotating columnar flow. The standard Navier Stokes solution does not exhibit a stagnation plane; however when pressure relaxation is included in the conservation equations, the emergence of a stagnation plane is readily apparent, even in this steady state-incompressible flow.

As shown in Appendix A, the theoretically-based pressure relaxation coefficient for air is a strong function of relative humidity. For dry air, the value of the pressure

relaxation coefficient is at least an order of magnitude larger than that of humid air. Consequently, for flows in humid air (tornadoes and cyclones.), the pressure relaxation coefficient is lower than pressure relaxation coefficients in dry air (e.g. dust devils). The role of the parameter $\eta_p \omega$ can be seen in Figures 5.1 – 5.7. Lower values of $\eta_p \omega$ produce a vortex that has a stagnation plane at much greater elevations than the stagnation plane for flows with larger values of $\eta_p \omega$. These observations are consistent with laboratory and field measurements (Hoecker, 1960; Ward, 1972; Golden, 1971) for such vortices. Typically, dust devils have stagnation plane altitudes measured in hundreds of meters (Sinclair, 1969), whereas tornadoes may have stagnation planes which extend thousands of meters (Hoecker, 1960). We can also infer that the magnitudes of the axial and radial components of these flows for small values of $\eta_p \omega$ are much smaller than the azimuthal components near the stagnation plane. The flow near the stagnation plane is dominated by the rotational component of the flow relative to the radial and axial components. Hoecker (1960) has observed that debris suspended in a tornado is lifted up and suspended in a funnel, appearing to hesitate aloft before being ejected outwards. When we observe the streamlines for cases where $\eta_p \omega$ is very small, this sort of phenomena can be explained.

Figure 5.7 shows that the rotating fluid column just below the stagnation plane loses its axial velocity. The flow just below the stagnation region appears to have the same structure and move upwards within a tight rigid core but when it approaches the stagnation plane, the flow turns outward and the axial velocity component decelerates to zero. At the stagnation plane, there is no more axial flow.

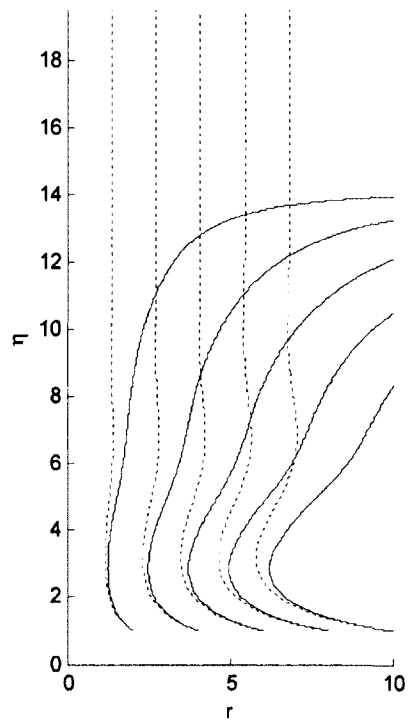


Figure 5.1 Streamlines through a vertical slice comparing Boedewadt solution (dashed line) and pressure relaxation solution with $\eta_p\omega=0.1$ (solid line)

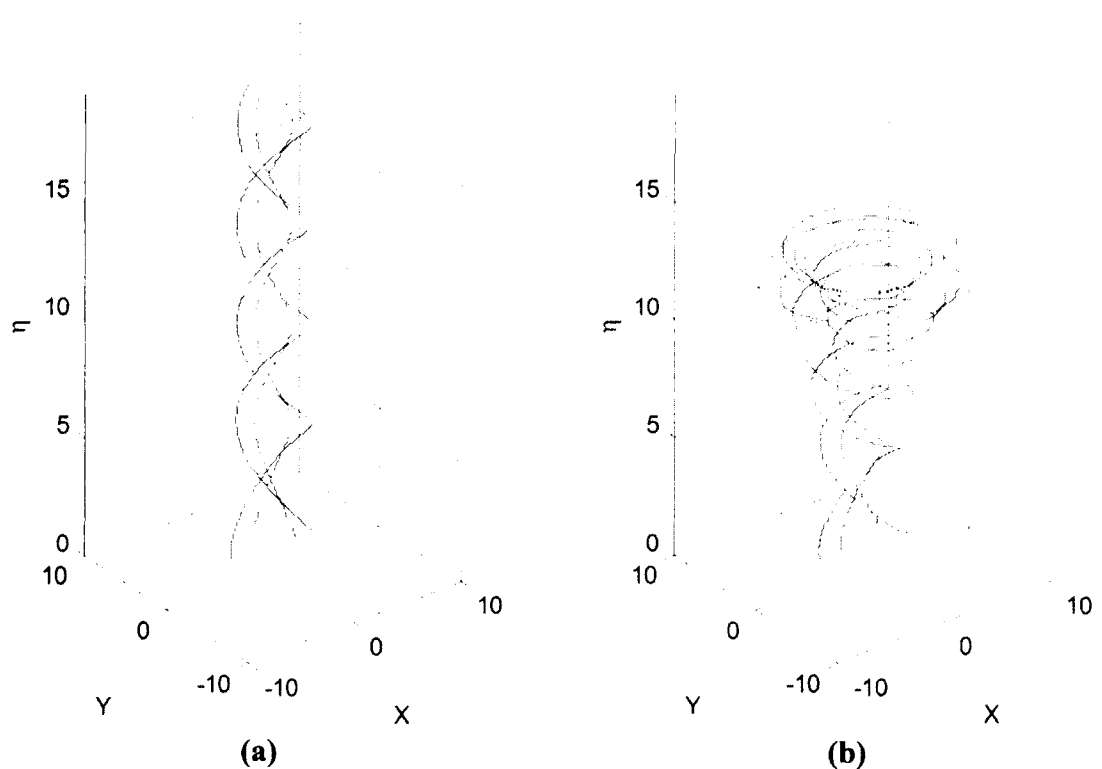


Figure 5.2: Streamlines patterns: (a) for Boedewadt Solution ($\eta_p\omega=0$), and (b) $\eta_p\omega=0.1$

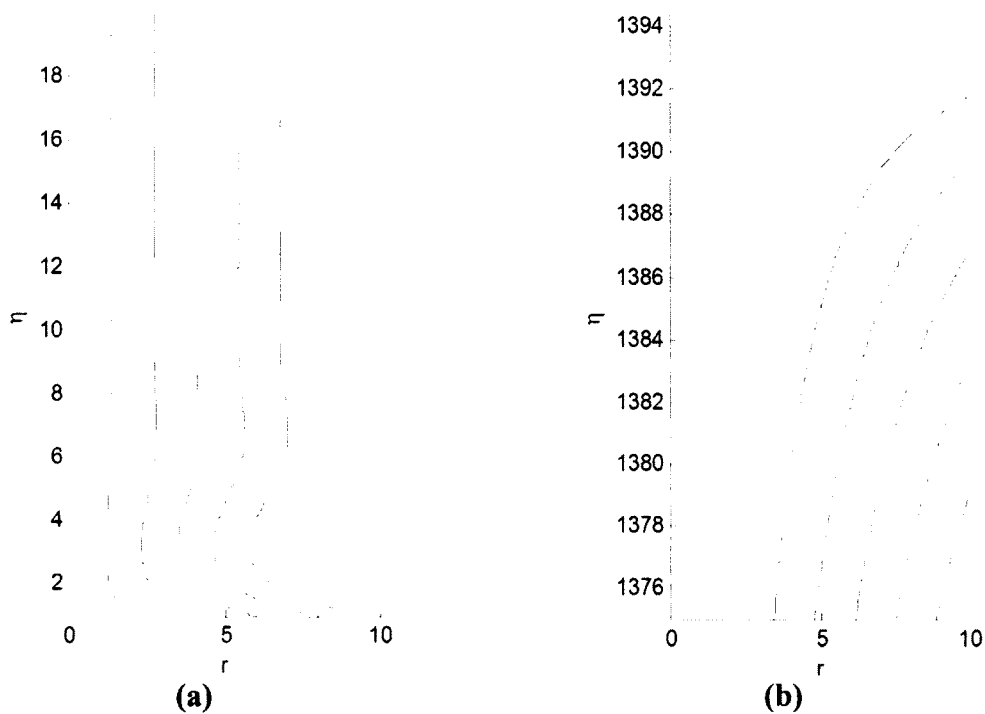


Figure 5.3 Streamlines through a vertical slice when $\eta_p\omega=0.001$ (a) near the ground (b) near the stagnation plane

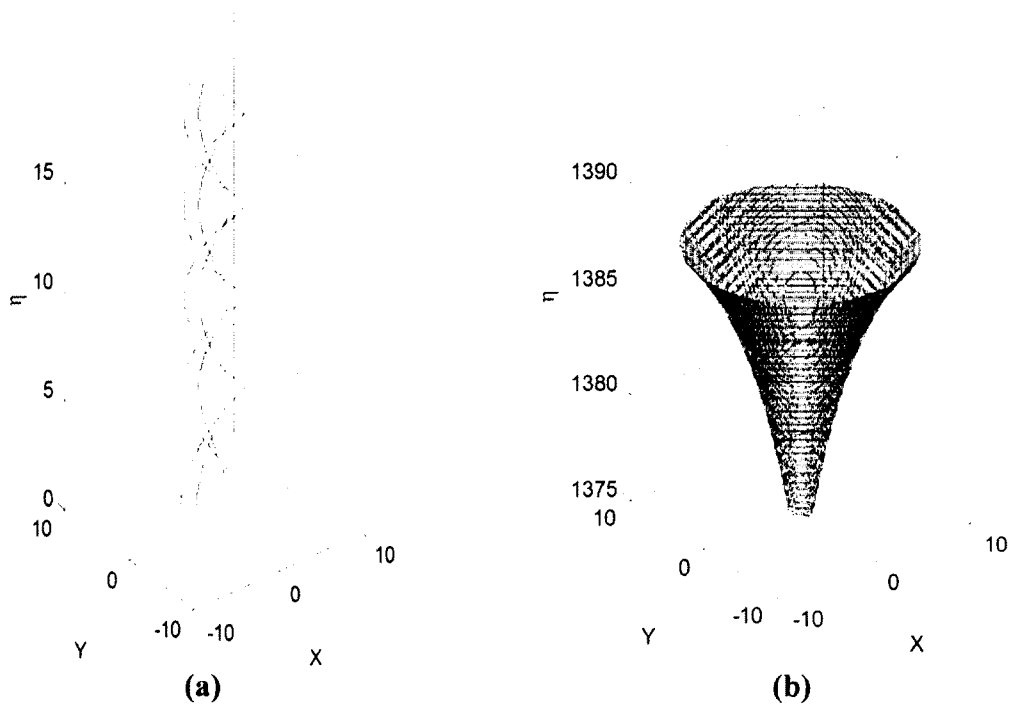


Figure 5.4 Streamlines with $\eta_p\omega=0.001$ (a) near the ground (b) near the stagnation plane

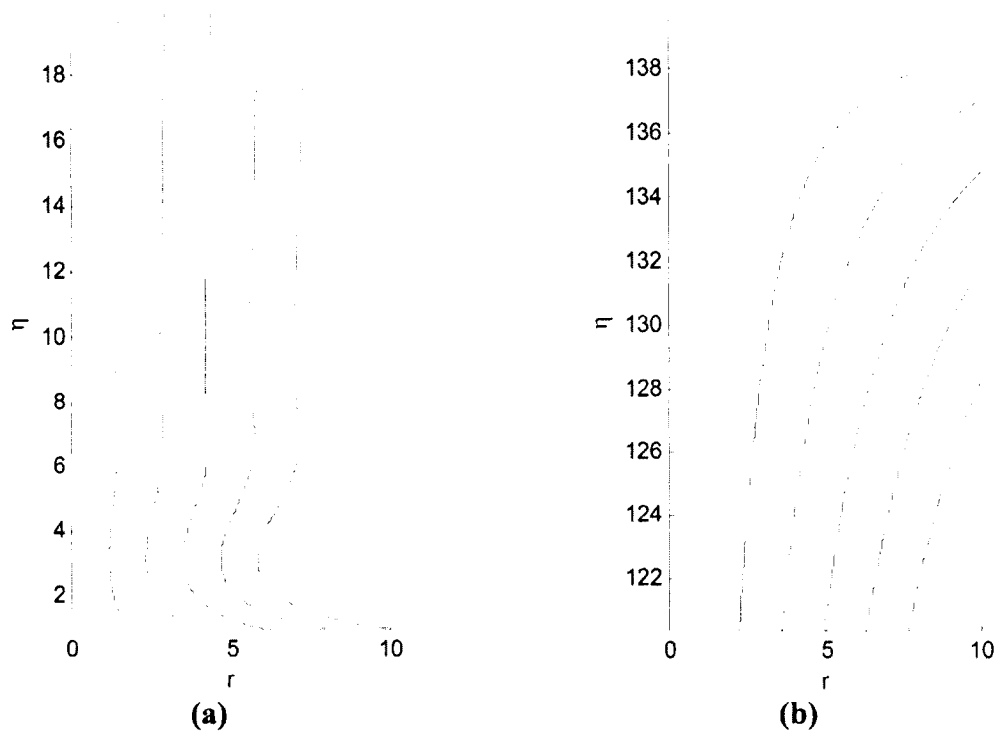


Figure 5.5 Streamlines through a vertical slice with $\eta_p \omega = 0.01$ (a) near the ground (b) near the stagnation plane

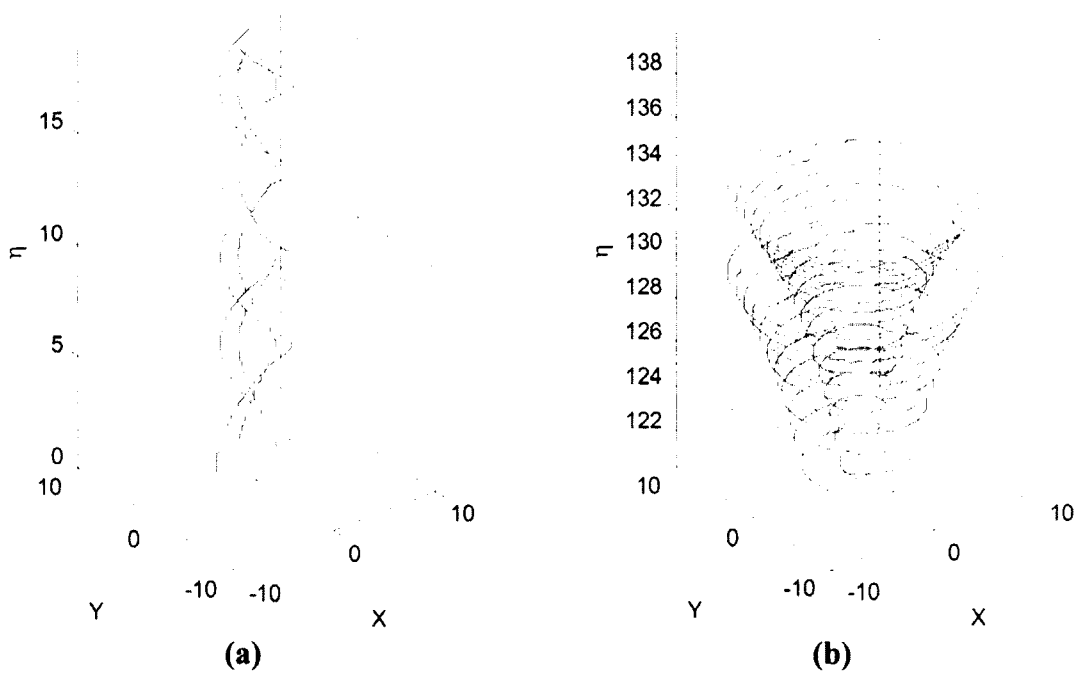


Figure 5.6 Streamlines with $\eta_p \omega = 0.01$ (a) near the ground (b) near the stagnation plane

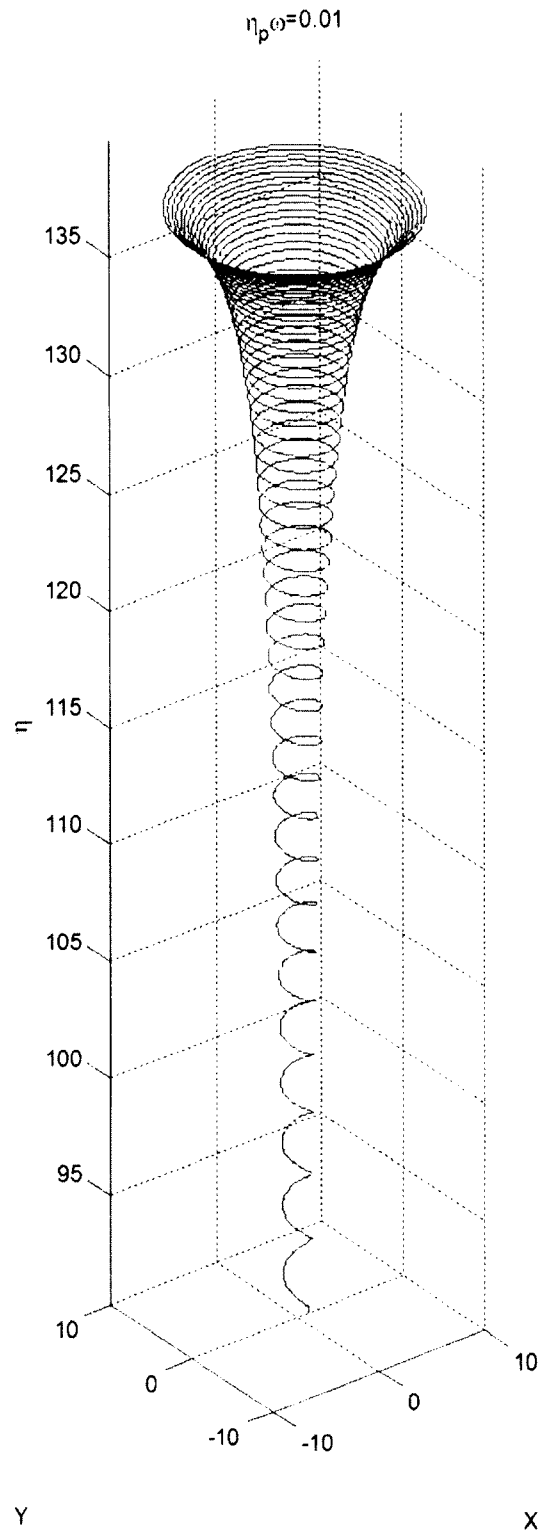


Figure 5.7 Streamlines with $\eta_p \omega = 0.01$ showing the rigid column below the stagnation plane

5.2 The Pressure Distribution

Figure 5.8 presents the pressure distribution within the rotating fluid column. The profile of the calculated pressure distribution within the column is in agreement with the measurements of Hoecker, (1961).

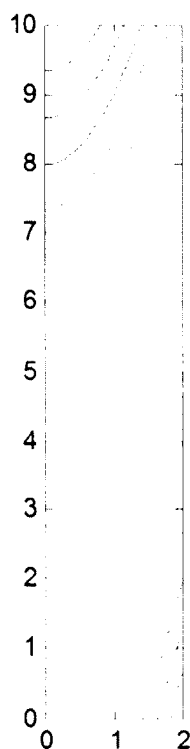


Figure 5.8 Pressure contours within the core

5.3 Determination of the Stagnation Plane Elevation

The stagnation plane above a rotating fluid column has been a focus of a number of studies (Bellamy-Knights, 1974), (Hatton, 1975), (Raymond & Rao, 1978). The existence of such a stagnation plane has also been observed in laboratory experiments (Ward, 1972) and in actual meteorological flows (Hoecker, 1960). It has been a general consensus that the stagnation plane is created by turbulence (Ward, 1972). In the

turbulent region, the axial flow component transitions from an updraft to a downdraft. So the stagnation plane is essentially a transition zone where the laminar and turbulent regions of the flow intersect.

Incorporating non-equilibrium pressure in the governing equations, the differential equations for the similarity functions can be integrated, employing various values for the scaling parameter, $\eta_p \omega$. It should be noted that the radial component of velocity approaches the asymptotic value, as discussed earlier in developing the far field boundary condition. The axial similarity function (H) tends toward a constant slope.

It was not possible to integrate the equations up to the stagnation point because of finite computer resources. The equations were integrated until the radial and azimuthal components of the flow reached their asymptotic values, to within a numerical tolerance. The axial velocity component attains a constant negative slope at this point. Using that constant slope, the location where the axial velocity component goes to zero can be determined, thus locating the stagnation plane (the stagnation plane is the location where the axial component of the flow is zero). This process was employed to locate the stagnation plane for a range of values of the parameter $\eta_p \omega$.

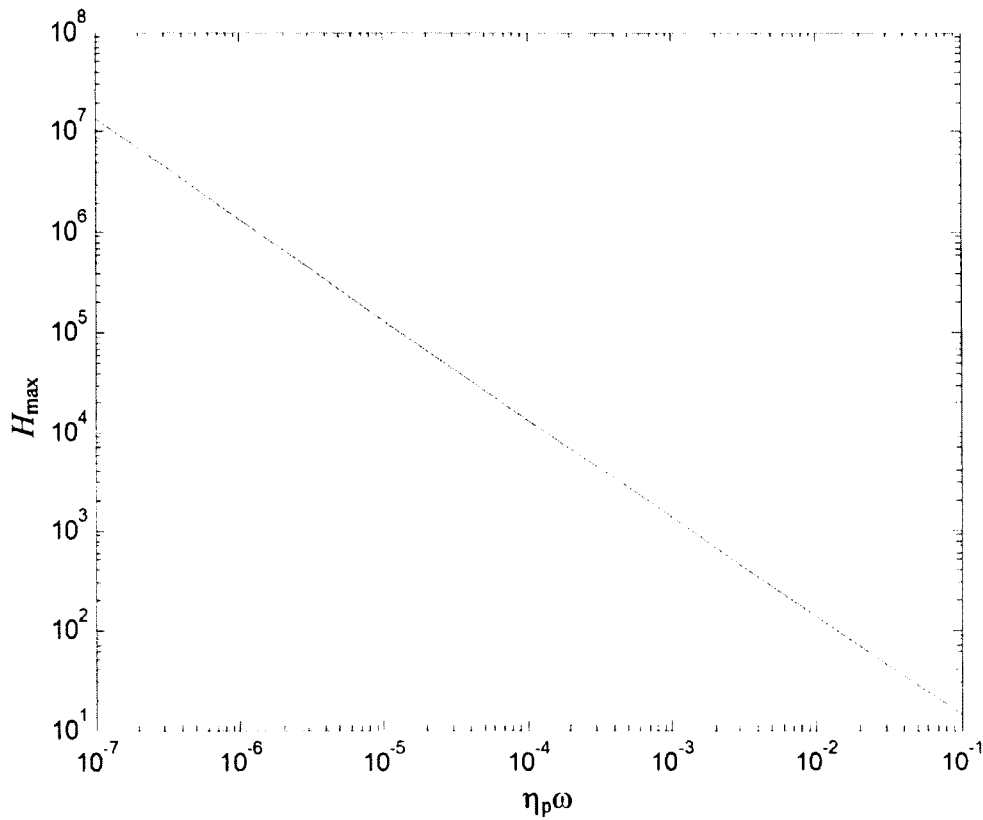


Figure 5.9 The location of the stagnation point vs. the parameter $\eta_p\omega$.

Figure 5.9 shows the relationship between the parameter $\eta_p\omega$ and the non-dimensional stagnation height, H_{\max} . A curve fit for the above figure produced the following relationship between the stagnation point and the non-dimensional height H_{\max} .

$$H_{\max} = \frac{1.394}{\eta_p\omega}, \quad (5.1)$$

where H_{\max} is the stagnation plane height. To find the physical separation height, the similarity variable η can be replaced using

$$z_{\max} = \frac{1.394}{\eta_p \omega} \sqrt{\frac{\nu}{\omega}}. \quad (5.2)$$

Using this relationship, the location of the stagnation point for a given rotating fluid column can be determined. Sinclair (1969) measured the core radii and the tangential velocities of dust devils in his earlier study. Table 3.2 contained the core radius, the maximum velocity and estimated pressure relaxation coefficient for the dust devils that were characterized in his study. The tangential component of flow away from the ground is similar to the tangential component of flow in an axial filament. Eq. (3.23) represents the tangential velocity profile for such flows and can be employed to develop a relationship between the angular velocity and the radial distance.

$$\omega(r) = \frac{2v_{\theta, \max}}{r_{\text{core}}} \frac{1}{(r/r_{\text{core}})^2 + 1} \quad (5.3)$$

The angular velocity on the centerline of the vortex can then be written in terms of the maximum swirl velocity and the core radius as

$$\omega_{\text{core}} = \frac{2v_{\theta, \max}}{r_{\text{core}}} \quad (5.4)$$

Using the data from Table 3.2, the estimated heights of the stagnation planes for the Sinclair dust devils have been summarized in Table 4.1.

Table 4.1 Stagnation heights for Sinclair (1969) Dust Devils

Case	η_p (μs)	r_{core} (m)	v_{max} (m/s)	ω_{core} (s^{-1})	v_{eff} (m^2/s)	Stagnation Height (m)
DD #1	1.049	2.3	11	10.26	7.1×10^{-5}	340
DD #2	1.125	2.6	12	9.24	7.1×10^{-5}	357
DD #3	1.092	3.35	8.8	5.25	6.2×10^{-5}	833

Sinclair (1969) has reported that the heights of the dust devil columns varied between a hundred meters and a thousand meters. Thus, the stagnation plane heights predicted by the present theory are within his estimates.

5.4 Limitations of the Solution

The central axial vortex volume has been assumed to be a near-rigidly rotating fluid column. Since away from the centerline of the vortex, these flows tend to behave like a free potential vortex, and the energy required to rotate a fluid column of very large radius becomes prohibitively large, the current solution cannot be applied to radially unbounded domains. The Rankine model (Rankine, 1869) and the Sullivan model (Sullivan, 1959), both assumed the inner core to have constant angular velocities; however, the Ash, Zardadkhan and Zuckerwar (2011) study showed that the inner angular velocity in the inner core was not a fixed constant. Equations 5.3 and 5.4 describe the distribution of the angular velocity and the core angular velocity. A non-dimensional angular velocity distribution, as a function of the non-dimensional radius, can then be written as

$$\bar{\omega}(\bar{r}) = \frac{1}{\bar{r}^2 + 1} \quad (5.5)$$

From this relation, it can be seen that the angular velocity is reduced to half the centerline angular velocity at the core radius. The solution cannot be used out to that radius. If it is assumed that the solution is valid to a radius where the angular velocity is approximately 90% of the angular velocity at the centerline, Equation 5.5 can be employed to estimate a limiting radius in terms of the core radius. That is, if

$$0.9 = \frac{1}{\bar{r}^2 + 1}, \quad (5.6)$$

the non-dimensional radius of the rigidly rotating column is

$$\bar{r} = 1/3. \quad (5.7)$$

Equation 5.7 shows that the solution is confined to a region which is one third the core radius, where the core radius is the radial distance where the swirl velocity is maximum. This corresponds to column diameters ranging from less than a meter for dust devils (Sinclair, 1969) to almost 100 meters for tornadoes and tens of kilometers for hurricanes.

5.5 Summary

The governing equations for fluid flow incorporating pressure relaxation predict the existence of a stagnation plane at the top of a rotating fluid column when the base of the column is required to satisfy no-slip boundary conditions. Axial up-flows and down-flows are present in tornado-like vortices. However, the height of the stagnation plane depends on the angular velocity and the magnitude of the pressure relaxation coefficient. Past theoretical findings of Hatton, (1975) and Raymond & Rao, (1978) suggest that such

vortices with a stagnation plane are transient and decay rapidly with time. Non-equilibrium pressure forces allow these vortices to exist as steady state vortices that can sustain themselves for much longer periods of time. While it wasn't possible to find reference data on the heights of tornado funnel clouds (locating the stagnation plane), the computed stagnation heights of dust devils incorporating pressure relaxation, were within observed limits (Sinclair P. C., 1964).

CHAPTER 6

CONCLUSIONS

6.1 Summary

The present study was undertaken to study the effects of non-equilibrium pressure on rotating flows with the objective of better understanding such flows. The governing equations of fluid flow were derived incorporating pressure relaxation effects by employing Hamilton's Principle of Least Action and including a conservation of reacting species constraint. It was shown that a pressure relaxation coefficient, η_p , can exist in fluid flow along with the conventional bulk/volume viscosity coefficient, η_v . The non-equilibrium pressure can control important fundamental flow processes because it provides a balancing mechanism for traditional equilibrium forces.

It was shown that non-equilibrium pressure effects can be present in fluids even when constant density constraints are applied to the fluid flow. An exact solution of the axisymmetric Navier Stokes equations with pressure relaxation was obtained for axial vortex filaments (Ash, Zardadkhan, & Zuckerwar, 2011). The resulting velocity and pressure distributions agreed with physical measurements for aircraft wake vortices, laboratory experiments, tornadoes and dust devils. Most of the observed flows were turbulent justifying kinematic viscosity values that were higher than the tabulated viscosities for air under similar conditions. For the case of axial vortex filaments, it was shown that pressure relaxation coefficient, η_p , along with the circulation and viscosity, can influence both the core radius and the maximum tangential velocity.

A similarity solution was developed for an axisymmetric rotating flow above a fixed ground plane. It was shown that this type of flow is controlled by a parameter that is the product of the far-field angular velocity and the pressure relaxation coefficient ($\eta_p \omega$). It was also shown that the height of a free-standing stagnation plane above a rotating fluid column depends on the same parameter. This dissertation has shown that even when a simple rotating fluid column velocity profile is subjected to a no-slip bottom boundary condition, the non-equilibrium pressure forces act to balance the viscous forces along the fixed boundary. However, when this flow is allowed to be three-dimensional, non-equilibrium pressure forces decrease away from the fixed boundary, leading ultimately to a stagnation plane whose height depends on the product of pressure relaxation coefficient and rate of angular rotation. In the absence of the pressure relaxation coefficient, the flow produced by a rotating fluid column above a ground plane has no stagnation plane.

This dissertation has established the importance of non-equilibrium pressure in controlling the heights of geophysical flows; specifically in predicting the appearance of a stagnation plane whose height is controlled by $\eta_p \omega$. This is consistent with a number of previous studies which suggest that the height of the stagnation plane depends on a parameter which is proportional to the angular velocity of the rotating column of fluid (Hatton, 1975; Raymond & Rao, 1978). The height of the stagnation plane was found to be inversely proportional to $\eta_p \omega$. Using the values of the pressure relaxation, viscosity and angular velocity, calculated for three documented dust devils, the height of the dust devil stagnation planes were estimated and found to be with experimentally-observed stagnation plane heights (Sinclair, 1969). The non-equilibrium pressure also plays an

important role in the formation of funnel shaped rotating columns in geophysical flows. The funnel is produced by decelerating axial flow in the presence of radial outflow.

6.2 Future Work

The current work can be extended in a number of ways in future studies of these types of flows. Firstly, the current work is limited to the nearly rigid core region of a columnar vortex. If the velocity profile of an axial vortex filament can be employed to describe the flow both in the viscous core and potential flow regimes, the similarity solution or a numerical solution can be used to model flows in all five regimes of rotating flows near the ground and the stagnation plane. Secondly, although the results of the current study are consistent with stagnation heights for dust devils, it is not possible to predict the stagnation planes for more complex flows like tornadoes and hurricanes due to important phase change and mass transport processes as well as the wide range of temperature and pressure zones that exist in such flows. Future work can include the impact of temperature and pressure changes along with the pressure relaxation to model tornadoes and hurricanes. Finally, since the current dissertation has already established the role of non-equilibrium pressure in fundamental flows, the role of non-equilibrium pressure can be studied for turbulent flows which may lead to better understanding of basic turbulent flow structures and improved modeling of turbulent flows.

REFERENCES

- ASH, R.L., ZARDADKHAN, I. & ZUCKERWAR, A.J. 2011. The influence of pressure relaxation on the structure of an axial vortex. *Physics of Fluids*, 23, 073101.
- BAKER, G.R., BARKER, S.J., BOFAH, K.K. & SAFFMAN, P.G. 1974. Laser anemometer measurements of trailing vortices in water. *Journal of Fluid Mechanics*, 65, 325-36.
- BALME, M. & GREELY, R. 2006. Dust devils on Earth and Mars. *Reviews of Geophysics*, 44, RG3003.
- BELLAMY-KNIGHTS, P.G. 1974. An axisymmetric boundary layer solution for an unsteady vortex above a plane. *Tellus*, 26, 318-24.
- BOEDEWADT, U.T. 1940 Die Drehströmung über festem Grunde. *Zeitschrift für Angewandte Mathematik und Mechanik*, 20, 241-53.
- BROOKS, H.B. 1959. Rotation of Dust Devils. *Journal of Meteorology*, 17, 84-86.
- BURGERS, J.M. 1948. A mathematical model illustrating the theory of turbulence. *Advances in Applied Mechanics*, 1, 171-99.
- BURNHAM, D.C. & HALLOCK, J.N. 1982. *Chicago monostatic acoustic vortex sensing system. Volume IV, Wake vortex decay*. Alexandria VA: National Technical Information Service.
- CASAS-VAZQUEZ, J. & JOU, D. 2003. Temperature in non-equilibrium states: a review of open problems and current proposals. *Reports on Progress in Physics*, 66, 1937-2023.
- CHILDS, P.R. 2011. *Rotating Flow*. Burlington, MA: Elsevier.
- DE GREGORIO, F. & RAGINI, A. 2003. Wake vortex characterisation in towing tank facilities using PIV technique. In *Proceedings of the 41st Aerospace Sciences Meeting and Exhibit*. Reno, NV, AIAA Paper No. 2003-93, 2003.
- DEGROOT, S.R. & MAZUR, P. 1962. Viscous flow and relaxation phenomena. In *Non-Equilibrium Thermodynamics*. North-Holland, Amsterdam: Dover Publications. pp.304-03.
- DELISI, D.P. et al. 2003. Aircraft wake vortex core size measurements. In *Proceedings of the 21st AIAA Applied Aerodynamics Conference*. Orlando, FL, 2003.
- DEVENPORT, W.J., RIFE, M.C., LIAPIS, S.I. & FOLLIN, G.J. 1996. The structure and development of a wing-tip vortex. *Journal of Fluid Mechanics*, 312, 67-106.

- GARODZ, L.J. & CLAWSON, K.L. 1993. *Vortex wake characteristics of B757-200 and B767-200 aircraft using the tower fly-by technique*. NOAA Technical Memorandum ERL ARL 199.
- GERZ, T., HOLZAPFEL, F. & DARRACQ, D. 2002. Commercial aircraft wake vortices. *Progress in Aerospace Sciences*, 38, 181-208.
- GOLDEN, J.H. 1971. Waterspouts and tornadoes over South Florida. *Monthly Weather Review*, 99, 146-54.
- GOVINDARAJU, S.P. & SAFFMAN, P.G. 1971. Flow in a turbulent trailing vortex. *Physics of Fluids*, 14, 2074-80.
- HATTON, L. 1975. Stagnation point flow in a vortex core. *Tellus*, 27, 269-79.
- HERIVEL, J.W. 1955. The derivation of the equations of motion of an ideal fluid by Hamilton's principle. *Proceedings of the Cambridge Philosophical Society*, 51, 344-49.
- HOECKER, W.H. 1960. Wind speed and air flow patterns in the Dallas tornado of April 2, 1957. *Monthly Weather Review*, 88, 167-80.
- HSU, C.T. & FATTAHI, B. 1976. Mechanism of tornado funnel formation. *Physics of Fluids*, 19, 1853-57.
- JACQUIN, L., FABRE, D., GEFFROY, P. & COUSTOLS, E. 2001. The properties of a transport aircraft wake in the extended near field: an experimental study. In *Proceedings of the 39th AIAA Aerospace Sciences and Exhibit*. Reno, NV, AIAA-2001-16827, 2001.
- KIERZENKA, J. & SHAMPINE, L.F. 2001. A BVP solver based on residual control and te MATLAB PSE. *ACM Transactions on Mathematical Software*, 27, 299-316.
- KOSIBA, K. & WURMAN, J. 2010. The three-dimensional axisymmetric wind field structure of the Spencer, South Dakota, 1998 tornado. *Journal of the Atmospheric Sciences*, 67, 3074-83.
- LAMB, H. 1932. *Hydrodynamics*. 6th ed. New York: Dover Publications.
- LEWELLEN, W.S. 1962. A solution for three-dimensional vortex flows with strong circulation. *Journal of Fluid Mechanics*, 14, 420-32.
- LILLY, D.K. 1969. *Tornado Dynamics*, National Center for Atmospheric Research, NCAR Manuscript No. 69-117.
- LONG, R.R. 1961. A vortex in an infinite viscous fluid. *Journal of Fluid Mechanics*, 11, 611-24.

- MCALISTER, K.W. & TAKAHASHI, R.K. 1991. NACA 0015 Wing pressure and trailing vortex measurements. In *NASA Technical Paper No. 3151 and AVSCOM Technical Report No. 91-A-003*.
- MCCORMICK, B.W., TANGLER, J.L. & SHERRIE, H.E. 1968. Structure of trailing vortices. *Journal of Aircraft*, 5, 260-67.
- MEIXNER, J. 1952. Allgemeine theorie der schallabsorption in gasen und flussigkeiten unter berucksichtigung der transporterscheinungen. *Acustica*, 2, 101.
- MOORE, D.W. & SAFFMAN, P.G. 1973. Axial flow in laminar trailing vortex. *Proceedings of the Royal Society of London A*, 333, 491-508.
- MORTON, B.R. 1966. Geophysical vortices. *Progress in Aerospace Sciences*, 7, 145-94.
- NEWMAN, B.G. 1959. Flow in a viscous trailing vortex. *Aeronautical Quarterly*, 10, 149-62.
- NOLAN, D.S. & FARRELL, B.F. 1999. The structure and dynamics of tornado-like vortices. *Journal of the Atmospheric Sciences*, 56, 2908-36.
- PROCTOR, F.H. 1998. The NASA-Langley wake vortex modelling effort in support of an operational aircraft spacing system. In *Proceedings of the 36th Aerospace Sciences Meeting and Exhibit*. Reno, NV, AIAA-1998-0589, 1998.
- RANKINE, W.J.M. 1869. *A Manual of Applied Mechanics*. 5th ed. London: Charles Griffin and Company.
- RAYMOND, W.H. & RAO, G.V. 1978. Boundary layer dynamics of a decaying core. *Tellus*, 30, 458-67.
- ROGERS, R.H. & LANCE, G.N. 1963. The boundary layer on a disc of finite radius in a rotating fluid. *The Quarterly Journal of Mechanics and Applied Mathematics*, 17, 319-30.
- ROTT, N. 1958. On the viscous core of a line vortex. *Zeitschrift für angewandte Mathematik und Physik*, 9b, 543-53.
- SCHLICHTING, H. 1968. *Boundary-Layer Theory*. 6th ed. New York: McGraw-Hill.
- SERRIN, J. 1959. Mathematical principles of classical fluid mechanic. In S. Flugge, ed. *Handbuch der physik*. 1st ed. Berlin: Springer-Verlag. pp.144-50.
- SERRIN, J. 1972. The swirling vortex. *Philosophical Transactions of the Royal Society A*, 271, 325-60.
- SHEKARRIZ, A., FU, T.C. & KATZ, J. 1993. Near-field behavior of a tip vortex. *AIAA Journal*, 31, 112-18.

- SINCLAIR, P.C. 1964. Some preliminary dust devil measurements. *Monthly Weather Review*, 92, 363-67.
- SINCLAIR, P.C. 1969. The lower structure of dust devils. *Journal of Atmospheric Sciences*, 30, 1599-619.
- SULLIVAN, R.D. 1959. A two-cell vortex solution of the Navier-Stokes equations. *Journal of Aerospace Science*, 26, 767-68.
- URBARZKA, E. & WILKEN, D. 1997. Estimating runway capacities of German airports. *Transportation Planning and Technology*, 20, 103-29.
- VELDHUIS, L.L.M., SCARANO, F. & WIJK, C.V. 2003. Vortex wake investigation of an Airbus A340 model using PIV in a towing tank. In *Proceedings of the 21st AIAA Applied Aerodynamics Conference*. Orlando, FL, 2003.
- WARD, N.B. 1972. The exploration of certain features of tornado dynamics using a laboratory model. *Journal of the Atmospheric Sciences*, 29, 1194-204.
- WHITHAM, G.B. 1963. The Navier-Stokes equations of motion. In L. Rosenhead, ed. *Laminar Boundary Layers*. Oxford: Clarendon Press. pp.124-27.
- WINCKELMANS, G.S., THIRIFAY, F. & PLOUMHANS, P. 2000 Effect of non-uniform wind shear onto vortex wakes: parametric models for operational systems and comparison with CFD studies. In *Handouts of the Fourth WakeNet Workshop on "Wake Vortex Encounter"*. Amsterdam, The Netherlands, 2000.
- WOODS, L.C. 1975. *The thermodynamics of fluid systems*. Clarendon: Oxford University Press.
- WOODS, L.C. 1996. *Thermodynamic inequalities in gases and magnetoplasmas*. Chichester: John Wiley and Sons.
- WOOD, V.T. & WHITE, L.W. 2011 A new parametric model of vortex tangential-wind profiles: development, testing and verification. *Journal of the Atmospheric Sciences*, 68, 990-1006.
- ZUCKERWAR, A.J. & ASH, R.L. 2006. Variational approach to the volume viscosity of fluids. *Physics of Fluids*, 18, 047101.
- ZUCKERWAR, A.J. & ASH, R.L. 2009. Volume viscosity in fluids with multiple dissipative processes. *Physics of Fluids*, 21, 033105.

APPENDICES

Appendix A. Pressure relaxation coefficient of air

The following method to determine the pressure relaxation coefficient is based on the method that was developed by Dr. A. Zuckerwar (Allan J. Zuckerwar, personal communication, January 6, 2011).

Input variables

Temperature T , K

Pressure P , atm

Relative humidity h_r , %

Constants

Gas constant = 8314.51 J/kmol.K = 82.0578337 atm.cm³/mol.K

Reference temperature $T_c = 273.16$ K

Reference pressure $P_R = 1$ atm

Vibrational Temp. N₂ = 3352.0 K

Vibrational Temp. O₂ = 2239.1 K

Mole fraction N₂ = 0.78084

Mole fraction O₂ = 0.20948

Rotational collision number $Z_{rot} = 5$

Mean free path (293 K) = 6.5×10^{-8} m

Molecular velocity (293 K) = 442.72 m/s

Mean free time (293 K) = 1.47×10^{-10} s

Rotational relaxation time (293 K) = $\tau_{rot}(293) = 5 \times \text{mft} = 7.34 \times 10^{-10}$ s

Derived variables

Saturation vapor pressure of water

$$\begin{aligned} \log_{10}(P_{sat}) = & 10.79586 [1 - (273.16/T)] \\ & - 5.02808 \log_{10}(T/273.16) \\ & + 1.50474 \times 10^{-4} \left\{ 1 - 10^{-8.29692 [(T/273.16)-1]} \right\} \\ & + 4.2873 \times 10^{-4} \left\{ -1 + 10^{4.76955 [1-(273.16/T)]} \right\} \\ & - 2.2195983. \end{aligned}$$

Mole fraction of water vapor

$$x_h = 0.01 h_r \frac{P_{sat}(T)}{P}$$

Normalized specific heat of N₂

$$\frac{C_N}{R} = (1 - x_h) \left(\frac{3352.0}{T} \right)^2 \frac{\exp\left(-\frac{3352.0}{T}\right)}{\left[1 - \exp\left(-\frac{3352.0}{T}\right) \right]^2}$$

Normalized specific heat of O₂

$$\frac{C_x}{R} = (1 - x_h) \left(\frac{2239.1}{T} \right)^2 \frac{\exp\left(-\frac{2239.1}{T}\right)}{\left[1 - \exp\left(-\frac{2239.1}{T}\right)\right]^2}$$

Normalized rotational specific heat

$$\frac{C_{rot}}{R} = 1$$

Relaxation frequency of N₂

$$f_N = \left(\frac{P}{P_R} \right) \left(\frac{T_0}{T} \right)^{1/2} [a_N(1) + a_N(2)x_h]$$

where

$$a_N(1) = 6.614 \times 10^4 \exp(-58.90T^{-1/3})$$

$$a_N(2) = 2.8 \times 10^4 \exp\left\{-4.170 \left[\left(\frac{T}{T_0} \right)^{-1/3} - 1 \right]\right\}$$

Vibrational relaxation time of N₂

$$\tau_N = 10^6 / (2\pi f_N) \text{ } \mu\text{s}$$

Relaxation frequency of O₂

$$f_x = (P/P_0^*) \left[a_x(1) + a_x(2)x_h \frac{a_x(3) + x_h}{a_x(4) + x_h} \right]$$

where

$$a_X(1) = 2.131 \times 10^5 \exp(-60.40T^{-1/3}) \text{ Hz}$$

$$a_X(2) = 4.04 \times 10^6 \text{ Hz}$$

$$a_X(3) = 16.46 \exp(-75.19T^{-1/3})$$

$$a_X(4) = 3.91 \times 10^{-3}$$

Vibrational relaxation time of O₂

$$\tau_X = 10^6 / (2\pi f_X) \text{ } \mu\text{s}$$

Rotational relaxation time

$$\tau_{rot} = \tau_{rot}(293) \times 10^6 \times (T/293)^{1/2} \text{ } \mu\text{s}$$

Rotational relaxation frequency

$$f_{rot} = 10^9 / (2\pi \tau_{rot}) \text{ Hz}$$

Pressure relaxation coefficient

$$\eta_p = \frac{x_N(C_N/R)\tau_N + x_X(C_X/R)\tau_X + (C_{rot}/R)\tau_{rot}}{x_N(C_N/R) + x_X(C_X/R) + (C_{rot}/R)} \text{ } \mu\text{s}$$

Table A.1 Pressure relaxation coefficient (in μs) for air at selected temperatures and relative humidities.

RH %	0	20	40	60	80	100
T, K						
273.15	43.38	2.58	1.31	0.88	0.66	0.53
283.15	50.52	1.78	0.91	0.61	0.46	0.37
293.15	58.23	1.28	0.64	0.43	0.32	0.26
303.15	66.50	0.93	0.47	0.31	0.23	0.18
313.15	75.31	0.69	0.34	0.23	0.17	0.13
323.15	84.64	0.52	0.26	0.17	0.12	0.10

Appendix B. The MATLAB Code

```

%% flowsol - Solver for the similarity equations
clc
clear
global ew;
ew=0.01;
solinit = bvpinit(linspace(0,20,50),@mat4init);
sol=bvp4c(@mat4ode,@mat4bc,solinit);
X1=sol.x;
F=sol.y(1,:);
G=sol.y(3,:);
H=sol.y(5,:);

plot(X1,F,'-k',X2,F2,':k',X3,F3,'--k')
xlabel('\eta');
ylabel('F');

figure
plot(X1,G,'-k',X2,G2,':k',X3,G3,'--k')
xlabel('\eta')
ylabel('G');

figure
plot(X1,H,'-k',X2,H2,':k',X3,H3,'--k')
xlabel('\eta')
ylabel('H');

%% the boundary conditions
function res = mat4bc(ya,yb)
global ew;
res = [ ya(1)
        ya(3)
        ya(5)
        yb(1)-ew/2;
        yb(3)-1 ];

%% initial guess
function yinit = mat4init(x)
yinit = [ -sin(x)/(x+1)
          -cos(x)/(x+1)
          sin(x)/(x+1)
          cos(x)/(x+1)
          cos(x)/(x+1)];

%% system of equations
function dydx = mat4odew(x,y)
ew=0.1;
dydx = [ y(2)
        (y(1)-ew)*y(1)-y(3)^2+y(5)*y(2)+ 1
        y(4)
        (2*y(1)-ew)*y(3)+y(5)*y(4)
        -2*y(1)];

```


VITA

IRFAN RASHID ZARDADKHAN

Old Dominion University
Norfolk, Virginia, 23529

EDUCATIONAL BACKGROUND

Ph.D. in Aerospace Engineering *August 2012*
Old Dominion University, Norfolk, VA, USA;

M.Sc. in Computing *June 2005*
University of Bahrain, Isa Town, Bahrain;

B.Sc. in Mechanical Engineering *January 2001*
University of Bahrain, Isa Town, Bahrain;

SELECTED PUBLICATIONS

ASH, R.L., ZARDADKHAN, I. & ZUCKERWAR, A.J. 2011. The influence of pressure relaxation on the structure of an axial vortex. *Physics of Fluids*, 23, 073101.